

## Noncollinear enhancement resonator with intrinsic pulse synchronization and alignment employing wedge mirrors

S. H. Wissenberg<sup>1,2,3</sup> J. Weitenberg<sup>1,4,\*</sup> J. Moreno<sup>4</sup> H. Hartung<sup>5</sup> M. Möslein,<sup>5</sup> Th. Burkhardt<sup>5</sup> T. Teschler<sup>2</sup> F. Schmid<sup>4</sup> Th. Udem<sup>4</sup> H.-D. Hoffmann<sup>1</sup> P. G. Thirolf<sup>3</sup> Th. W. Hänsch,<sup>4</sup> A. Ozawa<sup>4</sup> and C. L. Haefner<sup>1,2</sup>

<sup>1</sup>Fraunhofer-Institut für Lasertechnik ILT, Steinbachstr. 15, 52074 Aachen, Germany

<sup>2</sup>Lehrstuhl für Lasertechnik LLT, RWTH Aachen University, Steinbachstr. 15, 52074 Aachen, Germany

<sup>3</sup>Fakultät für Physik, Ludwig-Maximilians-Universität München (LMU), Am Coulombwall 1, 85748 Garching, Germany

<sup>4</sup>Max-Planck-Institut für Quantenoptik MPQ, Hans-Kopfermann-Str. 1, 85748 Garching, Germany

<sup>5</sup>Layertec GmbH, Ernst-Abbe-Weg 1, 99441 Mellingen, Germany



(Received 11 February 2025; accepted 1 April 2025; published 21 April 2025)

A noncollinear resonator with two beams circulating and intersecting in the focus allows resonator-assisted high-harmonic generation of high-power femtosecond pulses with efficient geometrical output coupling. However, the synchronization of the two pulses and alignment of the two beams is a challenge. We describe a resonator design employing wedge mirrors which avoids the need for separate mirrors for the two circulating beams, providing intrinsic synchronization and alignment. Transverse shifting of the wedge mirrors allows fine tuning the relative phase of the pulses, i.e., the interference pattern in the focus. We present the design of two noncollinear resonators at MPQ and at Fraunhofer ILT as well as the results of thorough characterization measurements on a noncollinear resonator with a low-power cw beam, demonstrating its versatility. We also include cylindrical mirrors into the resonator to adjust the ellipticity of the focus, which allows reducing cumulative plasma effects. Ellipticities  $\varepsilon > 3$  are reached without compromising the resonator enhancement of  $>50$ . The MPQ resonator has been designed for an EUV frequency comb at 60.8 nm to perform high-precision spectroscopy on the  $1s-2s$  two-photon transition in  $\text{He}^+$  ions for a test of quantum electrodynamics. The ILT resonator has been designed in the framework of developing a VUV frequency comb at around 148 nm envisaged as driver for the low-lying isomeric nuclear transition in  $^{229}\text{Th}$  (the so-called thorium isomer) as the presently only candidate for an ultra-high-precision nuclear frequency standard (“nuclear clock”).

DOI: [10.1103/PhysRevResearch.7.023071](https://doi.org/10.1103/PhysRevResearch.7.023071)

### I. INTRODUCTION

Enhancement resonators allow performing efficient high-harmonic generation (HHG) with high-repetition-rate ( $> 10$  MHz) laser systems, to produce spatially and temporally coherent radiation in the vacuum-ultraviolet (VUV) and extreme-ultraviolet (EUV) spectral range. A high repetition rate is beneficial for VUV/EUV frequency combs with resolvable comb modes and large power per comb mode, e.g., for precision spectroscopy, and for many other applications such as photoelectron spectroscopy, coherent imaging, and pump-probe experiments. A pulse train impinging on the resonator can be coherently enhanced by a factor 50 up to  $>1000$  to reach the high peak intensities required for HHG in a gas target despite the large repetition rate. This large enhancement is possible because of the small loss inside an enhancement resonator. A major challenge is to efficiently

output couple the harmonics, which are generated collinearly with the driving beam, while keeping the loss for the driving fundamental beam small, as there is no transparent material at short wavelengths. Several output-coupling schemes have been demonstrated that can be categorized in three groups displayed in Fig. 1: An element that transmits the fundamental beam [either under Brewster’s angle or as grazing-incidence plate (GIP) with an antireflection (AR) coating] but has some reflectivity for the generated harmonics, a grating that serves as highly reflective (HR) mirror for the fundamental but diffracts a part of the generated harmonics into different directions, and geometrical output coupling that uses the different beam divergence or spatial separation in the far field between the fundamental and the generated harmonics.

While the transmissive element is relatively simple in the implementation, it adds dispersion and nonlinearity to the enhancement resonator. A grating mirror overcomes these limitations [1]. Furthermore, the reflected harmonics are already spatially separated from the fundamental and from each other. Still, both methods are prone to degradation [2,3], introduce thermal lensing and limit the intensity by the damage threshold of the elements, as the output-coupling elements are close to the focus where HHG is taking place.

Geometrical output-coupling does not need additional elements in the beam path and has been realized with standard resonators featuring a mirror with a hole as collimation mirror

\*Contact author: johannes.weitenberg@ilt.fraunhofer.de

Published by the American Physical Society under the terms of the Creative Commons Attribution 4.0 International license. Further distribution of this work must maintain attribution to the author(s) and the published article’s title, journal citation, and DOI. Open access publication funded by Max Planck Society.

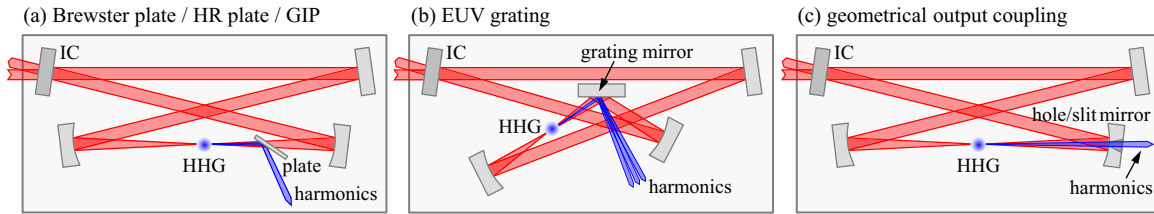


FIG. 1. Different possibilities for output coupling of the harmonics at resonator-assisted HHG: (a) separation of the harmonics via reflection at a plate at Brewster’s angle for the circulating radiation, possibly HR coated for the harmonics, or at a grazing-incidence plate (GIP) at larger angle, AR-coated for the circulating radiation, (b) separation via diffraction from a grating mirror, (c) separation exploiting the smaller divergence of the harmonics via geometrical output coupling (IC = input coupler).

[4–6], with degenerate resonators in which a circulating “slit mode” (combination of the Gauss-Hermite modes  $GH_{00}$  and  $GH_{40}$ ) has on-axis intensity close to the focus and avoids a slit in the collimating mirror (quasi-imaging) [7,8], and with noncollinear enhancement resonators [9]. In contrast to the other output-coupling methods, geometrical output coupling does not add dispersion, nonlinearity nor requires polarization discriminating elements, and its output-coupling efficiency increases for shorter wavelengths.

Geometrical output-coupling through a small hole in the collimating mirror becomes only efficient for higher harmonic orders, because of their smaller beam divergence. Another disadvantage is the high infrared (IR) intensity at edges of the hole when operated with the fundamental Gauss-Hermite ( $GH_{00}$ ) mode. The output coupling efficiency of resonators using a slit mode is larger [7] but it fixes the enhancement resonator to a defined position in the stability range (i.e., separation of the focusing and slit mirrors) to achieve degeneracy of transverse resonator modes. This determines the beam diameter on the resonator mirrors (for a given length) and limits scaling of the circulation peak power by the damage threshold of the mirrors. As the circulating slit mode has a rather complex beam profile, the spatial overlap with an impinging round or elliptical Gaussian beam is reduced compared to a circulating  $GH_{00}$  mode or it requires more involved mode matching. Noncollinear enhancement resonators combine the advantages of geometrical output-coupling with high output-coupling efficiency (already for lower harmonics) [9] and simple mode matching to a  $GH_{00}$  mode, but alignment difficulties have so far hindered their easy and widespread implementation. This work presents a compelling approach to noncollinear enhancement resonators by employing wedge mirrors instead of separate mirrors for the two circulating beams. These elements allow building a noncollinear enhancement resonator from monolithic mirrors, therefore greatly reducing the alignment effort, and providing intrinsic pulse synchronization and focus alignment. Furthermore, the relative phase of the two intersecting beams, and therefore the interference pattern in the HHG focus, is less prone to drifts.

The application that motivated this work is direct frequency-comb spectroscopy in the VUV and EUV spectral range, which can be reached via HHG of an IR frequency comb and particularly benefits from an enhancement resonator [10,11]. In addition to the power enhancement, the resonator suppresses phase noise which helps to avoid a carrier collapse [12–14]. These VUV/EUV frequency combs will serve as tools to reach our goals of performing a precise test

of quantum electrodynamics (QED) [15] and of building a nuclear clock which will allow tests of fundamental physics and search for dark matter [16]. The HHG enhancement resonator with efficient and power-scalable geometrical output coupling, which can be robustly implemented with a noncollinear geometry employing wedge mirrors, will therefore be a key ingredient to pushing our understanding of the physical world by allowing high-precision frequency metrology in the VUV/EUV [17].

## II. NONCOLLINEAR ENHANCEMENT RESONATOR

### A. Noncollinear HHG introduction

The idea of performing noncollinear HHG inside an enhancement resonator as a beneficial output-coupling scheme has already been suggested shortly after the first demonstration of resonator-assisted HHG in 2005 [18,19]: The proposed setups included an enhancement resonator of twice the length [20] or two separate enhancement resonators [21] [see Figs. 2(a) and 2(b)], aligned in a way that two pulses intersect in the focus. These design proposals have three main difficulties:

(1) Both resonators or resonator sections must have the same length such that the pulses temporally overlap in the focus, and the lengths must be kept constant up to a fraction of the wavelength to keep constructive interference on axis.

(2) Both resonators or resonator sections must be aligned for a spatial overlap of the two beams in the focal plane both longitudinally and transversely.

(3) The intensity distribution of the focus cannot easily be observed (via transmission through a resonator mirror) to monitor and adjust (1) and (2). The transmission of the two circulating beams through the separate focusing mirrors is not a copy of the reflected beams neither in phase nor in angle and therefore cannot serve as a monitor of the focus profile. The focus can also not be imaged through the separate collimation mirrors, as this would require the two substrates’ thickness to be identical on the subwavelength scale.

For the first demonstration of a noncollinear enhancement resonator for HHG, Zhang *et al.* [9] used a segmented input coupler (segment IC) to allow two spatially separated, circulating pulses to share two of the six enhancement resonator mirrors and therefore reduce complexity [Fig. 2(c)]. In their setup both the focusing and the collimating mirrors consist of two separated elements (one for each circulating beam) and therefore the difficulties (1–3) remain. An enhancement resonator without separate mirrors which supports two

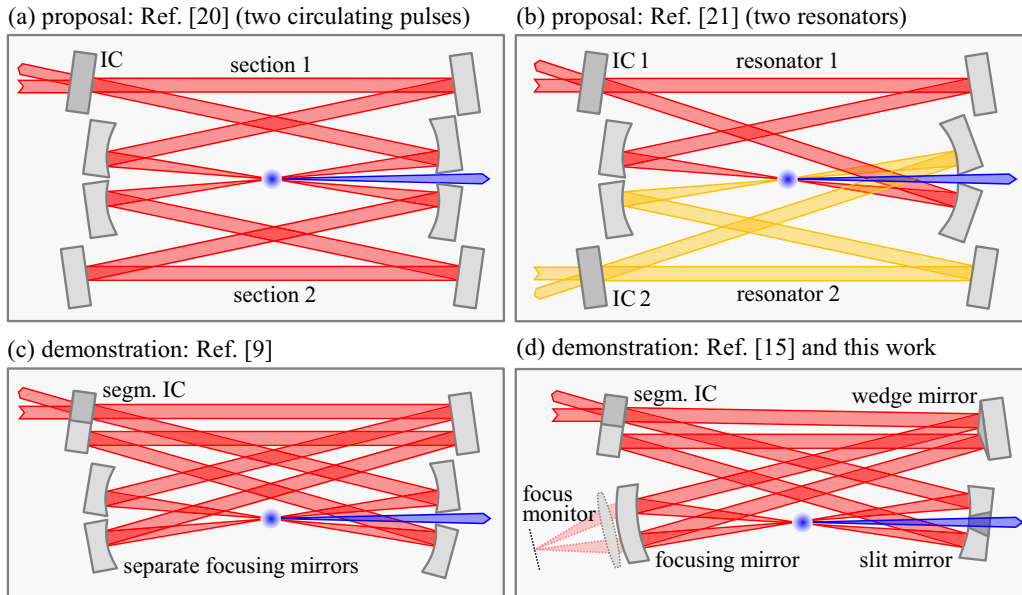


FIG. 2. Sketch of different possible geometries of a noncollinear HHG resonator: (a) two circulating pulses in a resonator with twice the length, (b) two resonators with intersecting foci (beams drawn with different color to distinguish the resonators), (c) two pulses circulating in a resonator with separate focusing mirrors while sharing others, (d) two pulses circulating and sharing all mirrors, enabled by at least one wedge mirror, providing intrinsic pulse synchronization and alignment (IC = input coupler). Note that a resonator which supports two circulating beams must contain separate mirrors for these beams or a wedge mirror, because it would otherwise not be stable. For a bow-tie resonator the beam would retrace its path after two round trips only if the resonator is operated at the confocal stability edge where the resonator eigenmode diverges.

circulating beams is not stable (it would have to be imaging with magnification  $-1$ ). This is the reason that the noncollinear resonator proposals and the first demonstration had to use separate mirrors for the two circulating beams. To overcome this limitation, we include special optical elements which we call “wedge mirrors” into the enhancement resonator. The wedge mirror consists of two plane segments which include an angle of  $2\gamma$  and which are optically contact bonded onto a common substrate and ultrashort-pulse laser-welded to form a monolithic element [see Fig. 3(b)]. The wedge mirrors replace the two optical surfaces of separate mirrors. With these wedge mirrors both circulating beams can use the same optical elements and therefore the pulses are intrinsically spatially aligned and temporally synchronized, solving difficulties (1) and (2). Furthermore, the leakage through the focusing mirror can be focused to a camera to monitor the interference pattern in the resonator focus, solving difficulty (3). Note that this “focus monitor” is not an image of the resonator focus but rather a copy [see Fig. 2(d)].

Apart from the noncollinear resonators shown in Fig. 2, also a resonator with a circulating  $GH_{10}$  mode and step mirrors which set the two lobes in phase to yield an on-axis maximum in the focus, as demonstrated in Ref. [22], can be called a noncollinear setup. In this reference, the step mirrors (in addition to a phase difference of  $\pi$ ) imprint a delay of the two lobes which leads to a wave-front rotation in the focus and to a different angle for the attosecond pulses from each half-cycle of the driving field (“attosecond lighthouse”). While this effect can be exploited to generate isolated attosecond pulses, it should be avoided here, highlighting the need to exactly synchronize the two circulating pulses in a noncollinear setup.

As a side remark: although a stable enhancement resonator with two circulating beams that share all the same optical surfaces is not possible, it is possible to build a stable enhancement resonator with three or four round trips before the beam reproduces itself by using a degenerate enhancement resonator with a Gouy parameter (the Gouy phase that the eigenmode accumulates at a resonator round trip, i.e., an eigenproperty of the resonator) of  $\psi_E = 4\pi/3$  or  $\psi_E = 3\pi/2$ , respectively. Using a degenerate resonator as a noncollinear enhancement resonator is closely related to quasi-imaging as an output-coupling method [23] and is also fixed to a certain position in the stability range.

## B. Noncollinear geometry

A noncollinear geometry is defined by two beams intersecting in the focus under the noncollinear angle  $\beta_{NC}$  (half angle), forming an interference pattern (Fig. 3). The pattern is determined by the noncollinear parameter  $\zeta = \beta_{NC}/\vartheta$ , which is the noncollinear angle  $\beta_{NC}$  divided by the far-field divergence angle  $\vartheta$  (half angle) of the beams. In the far field,  $\zeta$  is the relative beam displacement  $\delta = y_c/w$ , i.e., the displacement of the beams’ centroid from the optical axis  $y_c$  divided by the beam radius  $w$ . Therefore, a value  $\zeta \gtrsim 2$  must be chosen, to have a reasonable separation of the beams and small clipping loss in the resonator. Figure 3(a) shows a schematic noncollinear ring-resonator configuration. This configuration contains a wedge mirror and a segmented IC, which is a mirror that has a partially reflective (PR) coating on one half where the circulating pulse is supported by the impinging pulse train and a high reflective (HR) coating on the other half. The

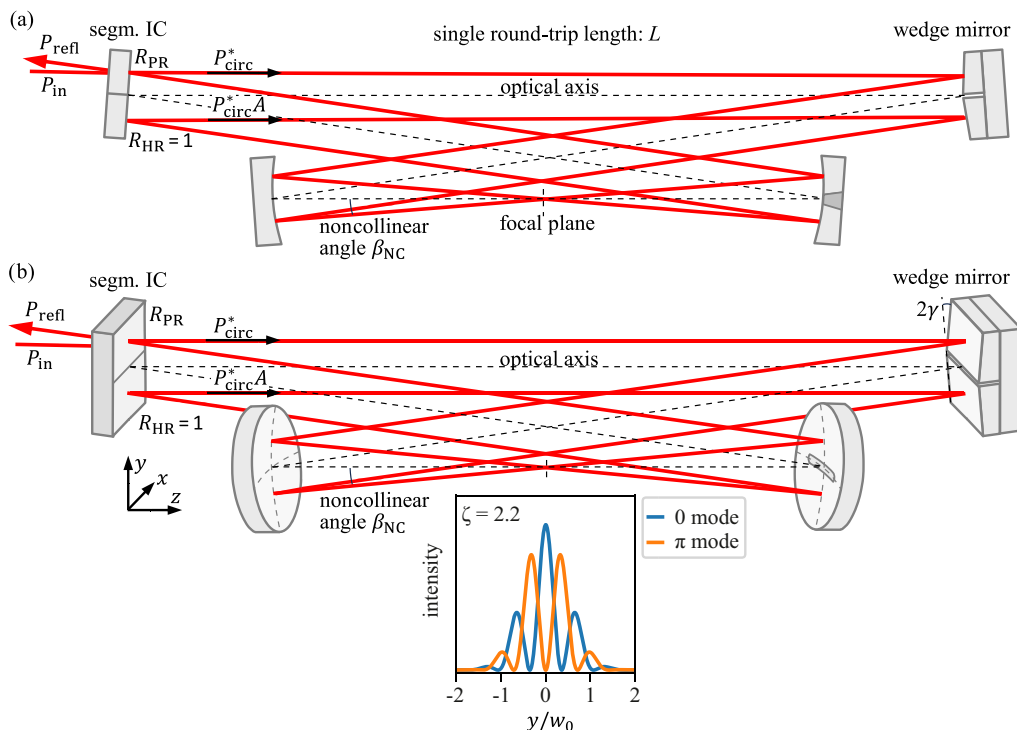


FIG. 3. Schematics of a noncollinear enhancement resonator with two circulating beams intersecting under an angle of  $2\beta_{NC}$ . The black dashed line depicts the optical axis of the resonator, the red lines depict the two circulating beams. The sketch visualizes the meaning of the impinging power  $P_{in}$ , the power reflected from the resonator  $P_{refl}$ , and the circulating power  $P_{circ}^*$  of a single beam.  $A$  is the loss factor for a single round trip.  $R_{PR}$  is the reflectivity of the partially reflecting segment of the segmented input coupler. The reflectivity of the other highly reflecting segment is assumed to be  $R_{HR} = 1$  for simplicity. The resonator contains a wedge mirror with wedge angle  $\gamma$ , which is half of the angle that the two reflective surfaces enclose. A noncollinear resonator can be realized in the following two ways: (a) resonator with the beams displaced in the resonator plane (top view); (b) resonator with the beams displaced perpendicular to the resonator plane (3D view). The inset shows the interference pattern in the focal plane if the circulating beams are in phase (0 mode) and out of phase ( $\pi$  mode) for a noncollinear parameter  $\zeta = 2.2$ .

middle line between the two circulating beams is the optical axis of the resonator (which we call “optical axis” for brevity). This term is meaningful to describe the resonator, although a geometric-optical beam cannot propagate along this line, as it would impinge on the apex (or the gap between the segments) of the wedge mirror. Throughout the manuscript we use  $z$  as the propagation coordinate along the optical axis,  $x$  as the transverse coordinate in the resonator plane and  $y$  as the transverse coordinate perpendicular to the resonator plane. The coordinate system shown in Fig. 3 (and the other figures) is only to remind that. It does not define the origin of the coordinates.

A noncollinear resonator is typically considered as a resonator with two pulses (two beams) circulating simultaneously and overlapping temporally while intersecting in the focus [9]. This picture lends itself when these beams use separate mirrors (possibly sharing some). In our situation, where the beams share all mirrors, it is also intuitive to think of a single circulating pulse with a single beam profile consisting of two lobes (or corresponding interference pattern in the focus). The two pictures make a difference when stating the circulating power  $P$  and enhancement  $E$ , which can either refer to a single beam or to the single profile with two lobes. We choose to refer to the power and enhancement of the single profile, which provides a more suitable comparison

between different output coupling schemes (noncollinear resonator,  $GH_{00}$ ,  $GH_{10}$ , slit mode). Still, we will refer to the two circulating beams in the manuscript when suitable. The power  $P^*$  and enhancement  $E^*$  of the single beams are introduced as auxiliary quantities and are marked with an asterisk.

In the following these quantities are used to evaluate the enhancement of the noncollinear resonator (see Fig. 3). Let  $A = 1 - l$  be the loss factor for a single round-trip with loss  $l$ , which contains all losses except for the input coupler, and  $R_{PR}$  the reflectivity of the PR segment of the input coupler. The reflectivity of the HR segment is assumed to be  $R_{HR} = 1$ . Note that loss, loss factor and reflectivity refer to the intensity of the beams, not to the field. The loss factor for two round trips then is  $A^* = A^2$ , and the power enhancement (on resonance) of a single beam  $E^*$  with the circulating power  $P_{circ}^*$  in a single beam can be written as (see, e.g., [24])

$$E^* = \frac{P_{circ}^*}{P_{in}} = U \frac{1 - R_{PR}}{(1 - \sqrt{R_{PR}A^*})^2}, \quad (1)$$

where  $P_{in}$  is the impinging power and  $U$  is the overlap of the impinging beam with the resonator mode. The circulating power in both beams (on resonance) is

$$P_{circ} = (1 + A) P_{circ}^* \approx 2 \sqrt{A} P_{circ}^*, \quad (2)$$

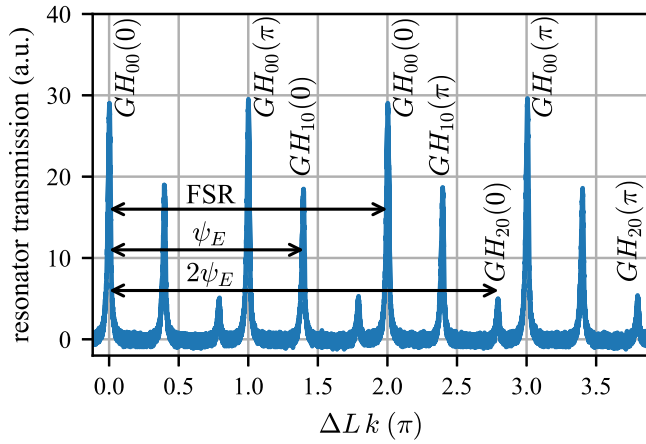


FIG. 4. Measured resonator transmission signal of a photo detector (PD) as a function of the resonator round trip phase of a noncollinear enhancement resonator. The impinging beam is intentionally slightly misaligned in the  $x$  direction to excite not only the fundamental Gauss-Hermite mode ( $GH_{00}$ ), but also the first two transverse higher modes  $GH_{10}$  and  $GH_{20}$ . The brackets indicate if the resonant mode is a 0 or a  $\pi$  mode. The distance between a resonant mode and the next transverse higher mode is given by the Gouy parameter  $\psi_E$ . The FSR corresponds to a phase of  $2\pi$  when considering a change  $\Delta L$  in the resonator length  $L$  acting on the beam with two lobes; it corresponds to a phase of  $4\pi$  when considering the phase of one Gaussian beam making two round trips (or when considering a change of the impinging beam frequency).

where we have used  $1 + A \approx 2\sqrt{A}$  assuming small loss. The corresponding resonator enhancement (on resonance) becomes

$$E = \frac{P_{\text{circ}}}{P_{\text{in}}} \approx U \frac{2\sqrt{A}(1 - R_{\text{PR}})}{(1 - \sqrt{R_{\text{PR}}A^2})^2} \approx U \frac{1 - \bar{R}_{\text{IC}}}{(1 - \sqrt{\bar{R}_{\text{IC}}A})^2}. \quad (3)$$

In the last approximation of Eq. (3) we introduced an effective input-coupler reflectivity  $\bar{R}_{\text{IC}} = \sqrt{R_{\text{PR}}}$ , which allows expressing  $E$  with the common equation for resonator enhancement. In the same way the coupling  $K$  to the resonator (on resonance) can be expressed as

$$K = 1 - \frac{P_{\text{refl}}}{P_{\text{in}}} = \frac{(1 - R_{\text{PR}})(1 - A^*)}{(1 - \sqrt{R_{\text{PR}}A^*})^2} = \frac{(1 - \bar{R}_{\text{IC}}^2)(1 - A^2)}{(1 - \bar{R}_{\text{IC}}A)^2}. \quad (4)$$

The coupling is  $K = 0$  for a lossless resonator ( $A = 0$ ) and  $K = 1$  for an impedance-matched resonator ( $\bar{R}_{\text{IC}} = A$ ).

If the round-trip length for both beams is equal, two distinct types of resonant modes (i.e., with round-trip phase a multiple of  $2\pi$ ) are possible: one where both beams are in phase and one in which both beams are out of phase. We call those modes 0 mode and  $\pi$  mode, respectively. The difference between 0 and  $\pi$  mode becomes visible in the focus of the short resonator arm, where both beams intersect: for the  $\pi$  mode the intensity vanishes on the optical axis, while the intensity profile of the 0 mode has a maximum on the optical axis (see inset of Fig. 3). Although driving HHG is possible with both modes [9], working with the 0 mode is desirable in our application, as then the generated harmonics have an almost Gaussian beam profile. In a resonator length scan (see Fig. 4)

the  $\pi$  modes correspond to the resonances that acquire a phase of  $\pi$  during a single round trip, which is possible because the resonator enhancement requires a phase of  $2\pi$  after two round trips. The fact that the circulating beam interferes with the impinging beam only after two round trips has another consequence: Gouy parameter values (for a single round trip) of  $\psi_E = 1.5\pi$  should be avoided, as then the second-order transverse mode of a  $\pi$  mode is degenerate with a fundamental 0 mode. In other words, the resonator becomes imaging after two round trips, i.e., it does not filter the circulating transverse mode. The resonator finesse  $F = \nu_{\text{FSR}}/\nu_{\text{FWHM}}$ , with the free spectral range  $\nu_{\text{FSR}}$  (frequency difference between two adjacent 0 modes) and the full-width-at-half-maximum linewidth of the resonator resonances  $\nu_{\text{FWHM}}$ , is (approximation for high finesse)

$$F \approx \frac{2\pi \sqrt{A\bar{R}_{\text{IC}}}}{1 - A\bar{R}_{\text{IC}}}. \quad (5)$$

Note that different approximations for the finesse (for high values) are used in literature. We could have, e.g., given  $F \approx \pi/(1 - \sqrt{A\bar{R}_{\text{IC}}})$  instead. As for the enhancement, using the effective input coupler reflectivity yields the same result as for a standard enhancement resonator. It is important to assign the proper value for the finesse to the noncollinear resonator, as it is needed to evaluate the optical bandwidth that the resonator supports and to describe limitations by plasma effects as discussed in Sec. II E. It follows from Eqs. (3) and (5) that the finesse is related to the enhancement of a noncollinear resonator in the same way as for a standard resonator.

The beam path of a noncollinear resonator can be in plane, i.e., the two beams are displaced in the direction of the resonator plane, as in Ref. [9] [and sketched in Figs. 2 and 3(a)]. The displacement of the beams can as well be perpendicular to the resonator plane (as sketched in Fig. 3(b) and in Fig. 5 of Ref. [15]). The latter is what we choose in our setups, motivated by the corresponding direction of the HHG gas jet, with the gas nozzle and the opposing gas catcher providing access and view from the top (perpendicular to the resonator plane). The resulting beam path is slightly out of plane, which raises two concerns: There could be a geometrical rotation of the beam including the direction of the electric field vector, which would mean that linear polarization is not an eigenstate (while circular polarization is) [25], and the eigenmode could exhibit general astigmatism including a twist [26]. Both concerns can be settled by simple considerations as well as by the experimental characterization presented in this paper. As all angles are small, the geometrical rotation is small, and for a symmetric resonator it vanishes after a round trip. The plane of incidence on the curved resonator mirrors is indeed tilted with respect to the resonator plane by a sizeable angle depending on the values of the noncollinear angle  $\beta_{\text{NC}}$  and the angle of incidence  $\alpha$  projected into the resonator plane, which we will use to describe the geometry. The actual angle in the plane of incidence is only slightly larger than  $\alpha$ . The tilted plane of incidence means that the difference in the effective focusing power in this plane and perpendicular to it (tangential and sagittal directions) represents a cylindrical focusing element which is not aligned with the transverse directions defined by the resonator plane. However, for small

angles of incidence, the difference in focusing power is small, and the focusing power describing the coupling between the transverse directions defined by the resonator plane is even smaller, e.g., corresponding to a focal length of 640 m for the resonator described in Sec. IV, which can be considered a small effect. The beam displacement is assumed in the  $y$  direction throughout the paper.

The electric field distribution in the focal and intersection plane ( $z = 0$ ) is determined by the phase difference  $\varphi$  between both beams and the noncollinear parameter  $\zeta$ . The mode of the beams is assumed to be stigmatic, i.e., no astigmatism and no ellipticity. An elliptical mode will be discussed in Sec. II F. The electric field (without time dependence) distribution in the focal plane with focus radius  $w_0$  reads

$$\mathcal{E}_{\text{NC}}(x, y, 0) = \sqrt{\frac{2}{c\epsilon_0}} \sqrt{\frac{4P}{\pi w_0^2}} \cos\left(2\zeta \frac{y}{w_0} + \frac{\varphi}{2}\right) \times \exp\left(-\frac{x^2 + y^2}{w_0^2}\right), \quad (6)$$

with the speed of light  $c$  and the vacuum permittivity  $\epsilon_0$ , and the intensity distribution is

$$I_{\text{NC}}(x, y, 0) = \frac{4P}{\pi w_0^2} \cos^2\left(2\zeta \frac{y}{w_0} + \frac{\varphi}{2}\right) \exp\left(-2\frac{x^2 + y^2}{w_0^2}\right). \quad (7)$$

A factor  $1 + \exp(-2\zeta^2) \approx 1$  in the normalization to the power  $P$  has been neglected. For the 0 mode ( $\varphi = 0$ ) the beam profile in the focus has an intensity maximum on the optical axis, while for the  $\pi$  mode the intensity is zero on axis and there are two fringes with equal intensity. Figure 5(a) depicts the intensity distribution and phase in the focus of both modes together with the intensity distribution on the slit mirror, i.e., in the far field, where the two beams are transversely separated and can avoid a slit for geometrical output coupling of harmonics generated in the focus.

The central fringe of the 0 mode can be approximated with a single (elliptical) Gaussian beam with the same on-axis intensity and the same shape around the maximum (defined by the same on-axis curvature of the intensity profile in the  $x$  and  $y$  directions). This criterion is motivated by the fact that at HHG only the high-intensity part of the profile contributes, while the low-intensity wings do not. The electric field  $\mathcal{E}'$  of this Gaussian “central-fringe beam” in the focal plane reads

$$\mathcal{E}'(x, y) = \sqrt{\frac{2}{c\epsilon_0}} \sqrt{\frac{2P'}{\pi w_{0,x} w'_{0,y}}} \exp\left(-\frac{x^2}{w_{0,x}^2} - \frac{y^2}{w'_{0,y}{}^2}\right), \quad (8)$$

with the power contained in this central-fringe beam  $P'$  and its beam waist radii  $w_{0,x}$  (same as for the circulating beam) and  $w'_{0,y} = w_{0,x}/\sqrt{1 + 2\zeta^2}$  in the  $x$  and  $y$  directions, respectively. The power fraction contained in the central-fringe beam is

$$\frac{P'}{P} = \frac{2}{\sqrt{1 + 2\zeta^2}} \quad (9)$$

and depends only on the noncollinear parameter  $\zeta$ . To reflect that the actual power in the central fringe is somewhat smaller than  $P'$ , it can be referred to as the “effective power” of the central fringe. Panels a, b, and c of Fig. 5 with the 0 mode

also include the intensity and phase distribution of the corresponding central-fringe beam. It can be seen that the slope of the on-axis phase at the focus is the same in both cases. This finding is not surprising, as according to the transport-of-intensity equations [27] the slope of the phase along the propagation direction  $\phi_0(z)$  is determined by the curvature of the transverse intensity profile (and vice versa the slope of the electric field amplitude  $\mathcal{E}_0(z)$  is determined by the curvature of the transverse phase profile):

$$\frac{\partial}{\partial z} \phi_0(z) = -\frac{1}{k} \frac{1}{\mathcal{E}_0(z)} \frac{1}{2} \left( \frac{\partial^2}{\partial x^2} + \frac{\partial^2}{\partial y^2} \right) \mathcal{E}(x, y, z)|_{x=y=0}. \quad (10)$$

The on-axis intensity along the propagation is given by (with  $z = 0$  in the focal plane)

$$I(0, 0, z) = \frac{I_0}{1 + z^2/z_R^2} \exp\left(-2\zeta^2 \frac{z^2/z_R^2}{1 + z^2/z_R^2}\right), \quad I_0 = \frac{4P}{\pi w_0^2} \quad (11)$$

with the on-axis intensity in the focus  $I_0$  and the Rayleigh length  $z_R$  of the (stigmatic) single beam. The FWHM focus length is shorter than for the single beam (along its beam axis), but it is longer than for the central-fringe beam. The different focus length and different course of the on-axis phase produce different conditions for HHG when comparing the noncollinear geometry to a Gaussian beam. Furthermore, the maximal intensity of the central-fringe beam (with reduced power, according to Eq. (9)) on the focusing and slit mirrors is smaller compared to the maximal intensity of the two noncollinear beams by a factor of  $(1 + 2\zeta^2)/4$  [see Fig. 5(a)].

### C. Resonator with wedge mirrors

For design considerations of a noncollinear enhancement resonator with wedge mirrors, it is instructive to look at the relative beam displacement  $\delta = y_c/w$  (distance of the beam to optical axis  $y_c$  divided by the beam radius  $w$ ) of the two circulating beams inside the resonator as a function of the accumulated Gouy phase  $\psi$  as the propagation coordinate instead of the propagation coordinate  $z$ . Consider a Gaussian beam (with beam-parameter product  $\text{BPP} = w_0\vartheta$ ) which propagates under an angle  $\beta_0$  with respect to the optical axis and with a displacement  $y_{c,0}$  at the beam waist at  $z = 0$  with Rayleigh length  $z_R = w_0^2/\text{BPP}$  and beam waist radius  $w_0$ . Using the relations  $\psi = \arctan(z/z_R)$ ,  $w = w_0\sqrt{1 + z^2/z_R^2}$  and  $\vartheta = w_0/z_R$ , the relative beam displacement  $\delta$  of this beam can be evaluated as a function of  $\psi$ :

$$\delta = \frac{y_c}{w} = \frac{\beta_0 z + y_{c,0}}{w} = \frac{\beta_0}{\vartheta} \sin(\psi) + \frac{y_{c,0}}{w_0} \cos(\psi). \quad (12)$$

Equation (12) is valid for free-space propagation, but it holds also for the propagation through an optical system that consists of free-space propagation and focusing elements. The relative beam displacement  $\delta(\psi)$  for each free-space section are connected at a focusing element in a continuous and continuously differentiable way, i.e.,  $\delta(\psi)$  is continued at such element. This is different from the evolution of the displacement  $y_c$  and of the beam radius  $w$  at a focusing element, which

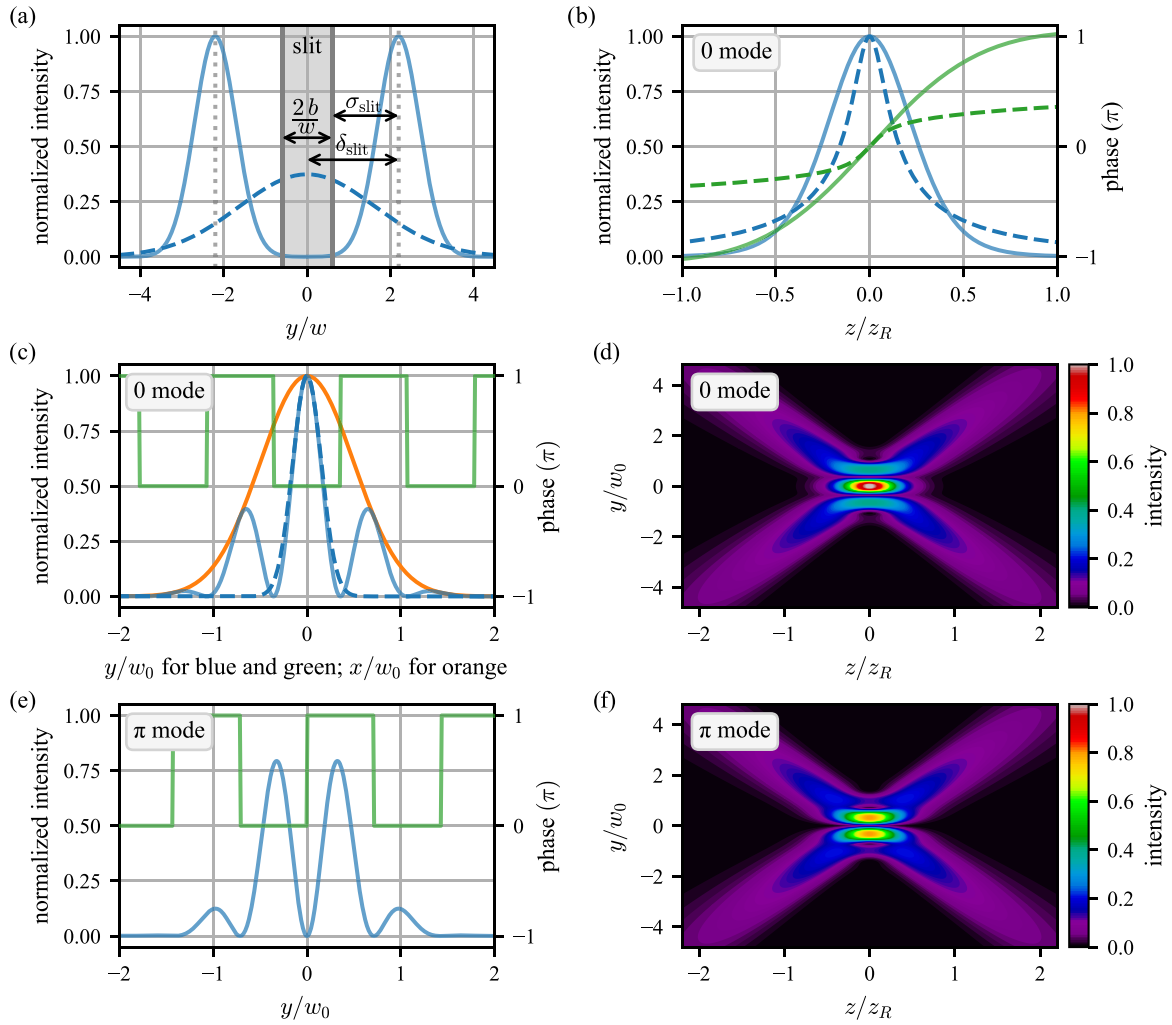


FIG. 5. Intensity distribution (blue and orange lines and color maps) and phase (green lines) of stigmatic noncollinear beams for 0 and  $\pi$  mode (solid lines) and the corresponding central-fringe beam (dashed lines) in the focus and on the slit mirror. Panel (a) shows the intensity distribution on the slit mirror for stigmatic noncollinear beams together with the (elliptical) central fringe beam. Furthermore, exemplary drawn are relative beam displacement  $\delta_{\text{slit}}$ , safety distance  $\sigma_{\text{slit}}$  and slit width  $b$  (half width,  $w$  is the beam radius on the slit mirror). Panels (b), (c), and (d) show a 0 mode at the focus: (b) on-axis intensity (blue) and on-axis phase (green) along the propagation direction  $z$  (phase in excess of a plane wave with the same wavelength), (c) intensity (blue and orange) and phase (green) along the transverse coordinates, and (d) intensity distribution in the  $y$ - $z$  plane. Panels (e) and (f) show a  $\pi$  mode at the focus: (e) intensity (blue) and phase (green) along the  $y$  direction, and (f) intensity distribution in the  $y$ - $z$  plane. All graphs are calculated for a noncollinear parameter  $\zeta = 2.2$ , which for the 0 mode corresponds to an effective power fraction of  $P'/P = 61\%$  in the central fringe. The intensity is normalized to the maximum intensity of the 0 mode.

are continuous at the element but not continuously differentiable. To show that  $\delta(\psi)$  is continuously differentiable, we investigate how the angle  $\beta$  evolves at propagation:

$$\beta = \frac{\partial}{\partial z} y_c = \frac{\partial}{\partial z} (\delta w) = w \frac{\partial}{\partial z} \delta + \delta \frac{\partial}{\partial z} w = \frac{\text{BPP}}{w} \frac{\partial}{\partial \psi} \delta + \frac{w}{R} \delta, \quad (13)$$

where the relations  $\frac{\partial}{\partial z} = \frac{\text{BPP}}{w^2} \frac{\partial}{\partial \psi}$  and  $\frac{\partial}{\partial z} w = \frac{w}{R}$  with the radius of curvature of the phase front  $R = z + \frac{z^2}{2R}$  have been used. Equation (13) can be rearranged to  $\frac{\text{BPP}}{w} \frac{\partial}{\partial \psi} \delta = \beta - \frac{w}{R} \delta$ . A focusing element with focal length  $f$  changes the angle  $\beta$  by  $-\frac{w}{f}$  and at the same time changes the curvature of the phase front

$\frac{1}{R}$  by  $-\frac{1}{f}$ , which means that the derivative  $\frac{\partial}{\partial \psi} \delta$  is unchanged, and therefore  $\delta(\psi)$  is continuously differentiable.

A wedge mirror changes the angle while not changing the radius of curvature. It therefore yields a discontinuity in the derivative of  $\delta(\psi)$  at the position of the wedge mirror, denoted with  $\psi_{\text{wedge}}$ . Following from Eq. (13), the value of the discontinuity of the derivative is related to the change in angle  $\Delta\beta$ , which is twice the wedge angle  $\gamma$ , as follows:

$$\Delta\beta = \frac{\text{BPP}}{w} \left[ \frac{\partial \delta}{\partial \psi} \Big|_{\psi_{\text{wedge}}^<} - \frac{\partial \delta}{\partial \psi} \Big|_{\psi_{\text{wedge}}^>} \right] = 2\gamma. \quad (14)$$

The simple function of the displacement in this picture allows easily constructing the displacement of the beams in a noncollinear resonator: Each segment between wedge

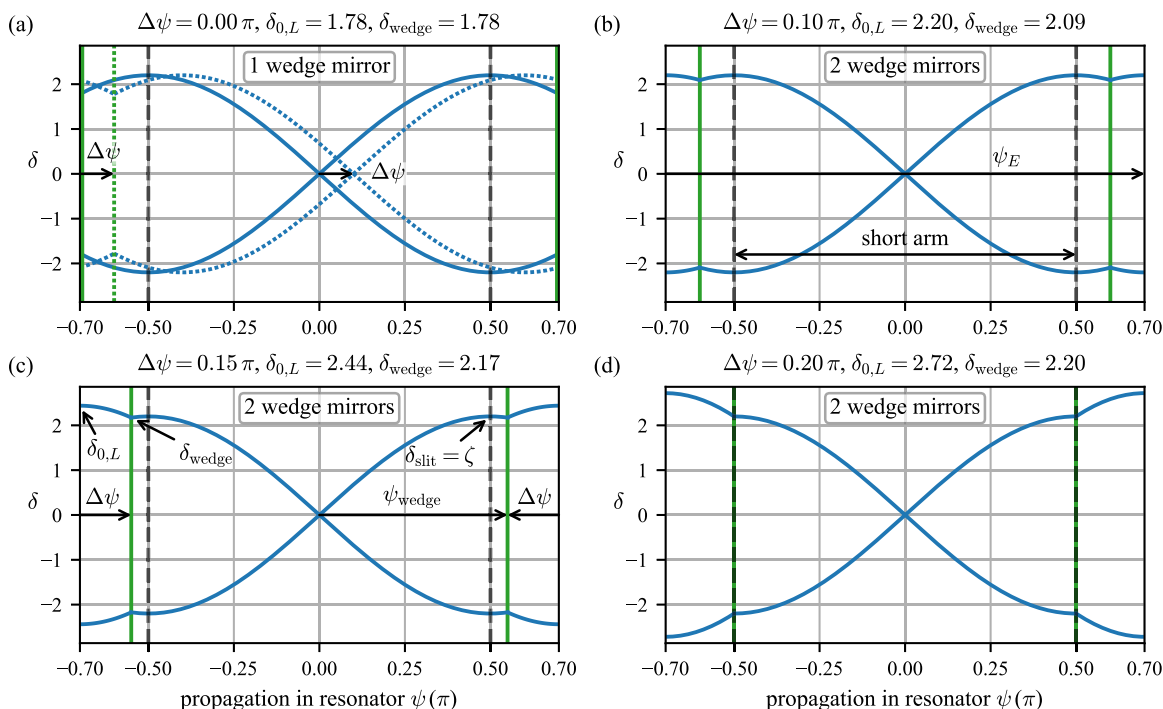


FIG. 6. Relative beam displacement  $\delta(\psi)$  as a function of the propagation in the resonator, given by the accumulated Gouy phase  $\psi$ , for different positions of the wedge mirrors in the long arm of a bow-tie resonator with  $\zeta = 2.2$  and  $\psi_E = 1.4\pi$ . A single round trip is completed after  $\psi$  increases by  $\psi_E$ , closing with a periodic boundary condition. The focus in the short arm is at  $\psi = 0$ , and the middle of the long arm is at  $\psi = \pm\psi_E/2$ . The wedge mirrors are positioned symmetrically at  $\pm\psi_{\text{wedge}}$  (green line,  $\Delta\psi$  away from the middle of the long arm), and the curved mirrors lie approximately at the gray dashed lines (which indicate the far field from the focus). Panel (a) shows the situation of only one wedge mirror placed in the middle of the long arm (solid lines) and the situation where this wedge mirror is placed  $\Delta\psi = 0.1\pi$  away from the middle of the long arm (dotted lines), resulting in a shift of the intersection plane from the focus by the same amount. In panels (b) and (c) two wedge mirrors are placed symmetrically around the middle of the long arm at increasing distance  $\Delta\psi$ , and finally in panel (d) the wedge mirrors are at the position of the focusing and slit mirrors. Note that the possible positions of the wedge mirrors can be constricted by the resonator design with a given number of mirrors. In situation (a) the relative displacement  $\delta$  on the wedge mirror (and possibly on the segmented input coupler placed in the long arm) is too small to safely avoid clipping; in situations (c) and (d) it is larger than necessary, which means that the PZT mirror (placed somewhere in the long arm) must be larger than necessary to fit the two beams. Situation (b) provides similar and suitable values for  $\delta$  on all mirrors. Panel (d) is similar to the situation of the noncollinear resonator of Ref. [9], where the pairs of focusing and collimating mirrors effectively take over the function of the wedge mirrors.

mirrors is described by a sine/cosine function, and at the wedge mirrors these functions must be connected in a continuous way but with a discontinuity in the derivative. If we demand a noncollinear geometry in the focus with a noncollinear parameter  $\zeta$ , then this yields a corresponding value of the discontinuity of the derivative, i.e., the wedge angle.

Consider a symmetric bow-tie resonator with the Gouy parameter  $\psi_E$  (which is determined by considerations on the beam radii in the focus and on the resonator mirrors), where the two beams are intersecting in the focal plane with noncollinear parameter  $\zeta$ . The intersection in the focal plane can be reached with a single wedge mirror in the middle of the long arm. Then Eq. (12) reduces to  $\delta(\psi) = \pm\zeta \sin(\psi)$  and describes the complete resonator, i.e., for  $-\frac{1}{2}\psi_E < \psi < \frac{1}{2}\psi_E$  with the focal plane at  $\psi = 0$ . The symbol  $\pm$  stands for the two circulating beams. This situation is plotted in Fig. 6(a).

If the wedge mirror is not exactly in the middle of the long arm, then the intersection point of the two beams shifts away

from the focus. The amount of this shift can be easily inferred from the construction of the function  $\delta(\psi)$ : Shifting the position of the wedge mirror by  $\Delta\psi$  [i.e., by the same fraction of the Rayleigh length in the respective arm; see Fig. 6(a)]. For a symmetric resonator setup, the wedge mirror cannot easily be placed in the middle of the long arm (compare Fig. 3). Even if the distance from the middle is rather large along the  $z$  coordinate, it can correspond to a small Gouy phase due to the large Rayleigh length in the long arm. While this shift of the intersection point might be acceptable, it seems reasonable to use two wedge mirrors symmetrically arranged around the middle of the long arm at a distance  $\Delta\psi$  each, to maintain the symmetry. Moreover, this allows reaching similar values of  $\delta$  on all mirrors, as can be seen in Fig. 6. With two wedge mirrors in a symmetric bow-tie resonator the beams between the wedge mirrors in the long arm are parallel to the optical axis, i.e., the relative beam displacement  $\delta(\psi)$  in this section is described by a cosine function. The relative beam displacement  $\delta(\psi)$  in this

resonator with noncollinear parameter  $\zeta$  is

$$\delta(\psi) = \begin{cases} \mp \delta_{0,L} \cos(\psi + \psi_E/2) & \text{for } -\psi_E/2 \leq \psi < -\psi_{\text{wedge}} \\ \pm \zeta \sin(\psi) & \text{for } -\psi_{\text{wedge}} \leq \psi < \psi_{\text{wedge}} \\ \pm \delta_{0,L} \cos(\psi - \psi_E/2) & \text{for } \psi_{\text{wedge}} \leq \psi < \psi_E/2 \end{cases}, \quad (15)$$

where the relative beam displacement in the middle of the long arm  $\delta_{0,L} = y_{0,L}/w_{0,L}$  corresponds to the ratio of beam displacement  $y_{0,L}$  at the beam waist position in the long arm and the respective beam waist radius  $w_{0,L}$ . Taking the sine/cosine functions in both resonator sections and fulfilling continuity at the wedge mirrors, yields the course of  $\delta$  in the complete resonator. This approach results in a relative beam displacement in the middle of the long arm of

$$\delta_{0,L} = \zeta \frac{\sin(\psi_{\text{wedge}})}{\cos(\psi_{\text{wedge}} - \psi_E/2)} \quad (16)$$

and a relative beam displacement at the wedge mirrors of

$$\delta_{\text{wedge}} = \zeta \sin(\psi_{\text{wedge}}). \quad (17)$$

Panels a–d in Fig. 6 show  $\pm\delta(\psi)$  for different values of  $\psi_{\text{wedge}}$ . The wedge angle  $\gamma$  of each of the wedge mirrors required to reach the noncollinear parameter  $\zeta$  can be calculated by

$$\gamma = \zeta \frac{\text{BPP} \cos(\psi_E/2)}{4 w_{0,L}}. \quad (18)$$

Note that  $\gamma$  is independent of the position of the wedge mirror in the long arm.

We want to choose  $\Delta\psi$  in a way that the beam displacement on the wedge mirrors  $\delta_{\text{wedge}}$  is sufficiently large to avoid clipping the beams on the apex of the wedge mirrors. On the other hand, the absolute beam size and beam separation should be small at the position of the PZT mirror, which is needed for resonator-length stabilization and must be placed somewhere in the long arm. Such a mirror (a mirror glued onto a PZT element) is designed to be small and light to enable a large stabilization bandwidth, and therefore a small beam displacement on the PZT mirror  $\delta_{\text{PZT}}$  together with a small beam size is helpful. We find a configuration close to  $\Delta\psi = 0.1\pi$  [Fig. 6(b)] for a resonator with Gouy parameter  $\psi_E = 1.4\pi$  a good compromise with placing the PZT mirror close to the beam waist in the long arm. Note that this configuration with a small beam displacement  $\delta$  in the long arm is only possible with carefully designed optics, like wedge mirrors with a very small gap and a segmented input coupler with a very small transition width between the two corresponding segments (see Sec. IV A for a characterization of the resonator optics).

According to Eq. (18) the required wedge angle  $\gamma$  is determined by  $\zeta$  and  $\psi_E$  and is plotted in Fig. 7. The noncollinear parameter  $\zeta$  is chosen as a compromise between the power contained in the central fringe in the focus and the output-coupling efficiency. That means that  $\gamma$  must be chosen according to the position in the stability range at which we want to operate the enhancement resonator. Therefore, for a given wedge angle the resonator is quite inflexible in terms of adapting the focus intensity by changing the position in the stability range, i.e.,  $\psi_E$  [23,28].

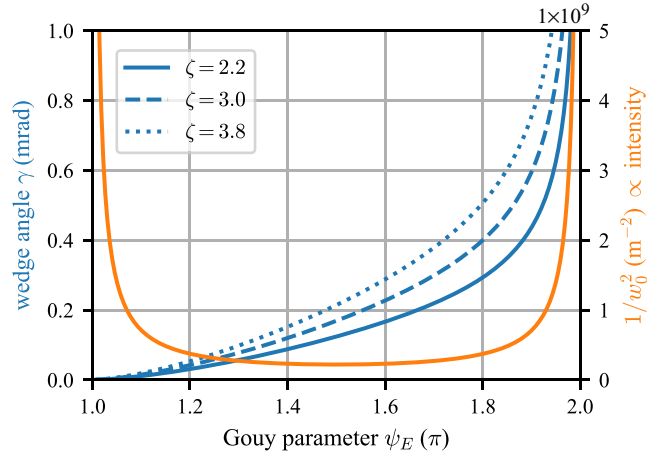


FIG. 7. Wedge angle  $\gamma$  and intensity in the focus as a function of the Gouy parameter  $\psi_E$  (position in the stability range) of a symmetric bow-tie resonator. When  $\gamma$  is fixed, a change of the position in the stability range goes along with a change of  $\zeta$ . The curves are calculated for a resonator length  $L = 7.5$  m, mirrors with ROC = 600 mm, and the wavelength  $\lambda = 1 \mu\text{m}$ .

In a real noncollinear resonator, the round-trip lengths of the two circulating beams will not be exactly equal because of a possible phase difference upon reflection on the segmented input coupler or a height difference between the two segments of the wedge mirror. The phase difference between the two beams results in resonant modes that are not 0 or  $\pi$  modes but with some other phase, i.e., these modes do not have the intensity maximum or minimum on axis at the beam intersection on axis. One can adjust the phase by placing one of the wedge mirrors on a translation stage for the direction of the beam displacement ( $y$  direction).

#### D. Estimation of HHG output-coupling efficiency

The output-coupling efficiency of a noncollinear HHG resonator can be estimated and compared to other geometrical output-coupling schemes using a simple model for the HHG process: The harmonics are assumed to be generated in a single transverse plane in (or close to) the focus. The phase front of the harmonics is assumed to be the same as that of the driving field, i.e., the intensity dependence of the harmonic phase is neglected, and the beam radius of the harmonics is calculated from the driving intensity profile assuming an intensity dependence with an exponent  $q$ , i.e., the harmonic intensity is  $I_H(x, y) \propto I^q(x, y)$  with the driving intensity  $I(x, y)$ . This yields a beam radius of the harmonics which is smaller than the driving beam radius by a factor  $\sqrt{q}$ . In perturbation theory the exponent is given by the harmonic order  $q = H$ . While this does not hold for high harmonic orders, we still use this assumption for a rough comparison, as it does capture the scaling of divergence and output-coupling efficiency with the harmonic order. The beam-parameter product (focus radius times divergence angle)  $\text{BPP}_H = w_{0,H} \vartheta_H \propto 1/H$  is smaller for higher harmonic orders due to the smaller wavelength; at the same time the focus radius  $w_{0,H} \propto 1/\sqrt{q}$  is smaller for higher harmonic orders due to the stronger intensity dependence. As the latter effect is weaker, the divergence of

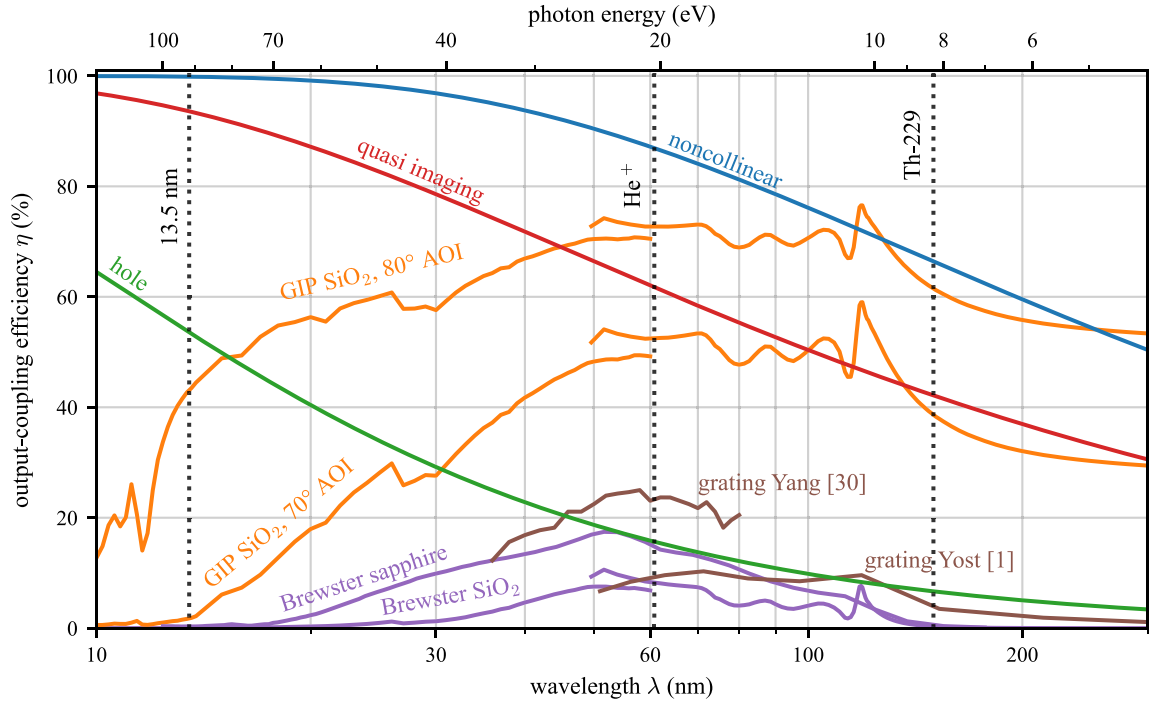


FIG. 8. Output-coupling efficiency vs wavelength (lower axis, log. scale) or corresponding photon energy (upper axis, log. scale) of the harmonics for different output-coupling schemes. A driving wavelength of  $1 \mu\text{m}$  is assumed. Orange curves: Reflectivity of a grazing-incidence plate (GIP) with fused silica ( $\text{SiO}_2$ ) as the top-layer material of the anti-reflection coating at  $70^\circ$  and  $80^\circ$  angle of incidence (AOI) for  $s$  polarization. Note that for wavelengths  $>130 \text{ nm}$  the assumption is not valid that the reflectivity is given by the  $\text{SiO}_2$  top layer alone. For these wavelengths it is possible to use a dielectric coating under a suitable angle (e.g., Brewster's angle) with high reflectivity for a specific harmonic order, e.g., reaching 75% for  $p$  polarization at  $149 \text{ nm}$  [2]. Purple curves: Reflectivity of (uncoated) plates at Brewster's angle ( $60^\circ$  for sapphire,  $56^\circ$  for fused silica) for  $p$  polarization. Brown curves: Reflectivity of grating mirrors stated by Yost *et al.* [1] ( $70^\circ$  AOI,  $s$  polarization, calculated values) and Yang *et al.* [30] ( $72^\circ$  AOI,  $s$  polarization, measured values). For calculating the geometrical output-coupling efficiency curves according to the simple model described in the main text  $q = H$  is assumed, and the following parameters are used: noncollinear resonator: noncollinear parameter  $\zeta = 2.2$  (ratio of the noncollinear angle and the far-field divergence angle of the intersecting beams), safety distance  $\sigma_{\text{slit}} = 1.6$  (ratio of the distance from the beam to the edge of the slit and the beam radius); hole mirror and fundamental mode: 1% clipping loss (allowing an enhancement of 50); quasi-imaging:  $b/w = 0.2$  (ratio of half slit width  $b$  and beam radius  $w$ ). The dimensions of the slit and hole are chosen for reasonable operation conditions of the respective scheme. Material parameters are taken from Ref. [31]. Dotted vertical lines mark the wavelengths needed to drive the thorium nuclear-clock transition (Th-229,  $148.4 \text{ nm}$ ) and the  $1s$ - $2s$  transition in singly ionized helium ( $\text{He}^+$ ,  $60.8 \text{ nm}$ ), as well as the EUV lithography wavelength ( $13.5 \text{ nm}$ ) as a reference.

the harmonics is smaller for higher harmonic orders; assuming  $q = H$  it scales as  $\vartheta_H \propto 1/\sqrt{H}$ . This relationship corresponds to a larger efficiency at geometrical output-coupling for higher harmonic orders compared to lower harmonic orders and contrasts with output-coupling via dielectric elements or gratings, where the efficiency becomes smaller for higher harmonics. This simple model yields an output-coupling efficiency for a noncollinear HHG resonator (0 mode) of

$$\eta_{\text{NC}} = \text{erf} \left( \sqrt{2} \frac{\zeta - \sigma_{\text{slit}}}{\sqrt{1 + 2\zeta^2}} \frac{H}{\sqrt{q}} \right) \quad (19)$$

with the safety distance  $\sigma_{\text{slit}} = (y_{\text{slit}} - b)/w_{\text{slit}}$  of the beams to the slit of width  $2b$  [see Fig. 5(a)]. To derive Eq. (19) the 0 mode is approximated with the central-fringe beam. More detailed calculations of the output-coupling efficiency can be found in Refs. [5,7,13]. A comparison of the output-coupling efficiency of the noncollinear HHG resonator to the fundamental mode with a hole mirror, the slit mode with slit mirror

[8], grazing-incidence plates (GIP) [29], Brewster plates, and grating mirrors is shown in Fig. 8.

### E. Estimation of loss due to HHG plasma

The HHG process goes along with a partial ionization of the gas target and the resulting plasma imprints a phase onto the circulating beam. This phase can be thought of as an aberration on the circulating mode and leads to on-axis intensity at the position of the slit mirror and to additional resonator loss. For the following discussion only the 0 mode is considered, and its central fringe is approximated by the central-fringe beam introduced in Sec. II B, to find the scaling behavior of the loss caused by the HHG plasma and to estimate the power of the fundamental laser field leaking through the output-coupling slit.

Assuming an ionization rate proportional to the intensity raised to the power of  $p$ , the phase profile is given by a Gaussian profile with radii smaller by a factor  $\sqrt{p}$  compared to the intensity profile. Here only the ionization within a single pulse

is considered. For the cumulative plasma effect (see Sec. II F), additionally the flow of the ionized gas can be considered. With the on-axis phase (at the end of the pulse)  $\phi_{\max}$  the phase profile is

$$\phi_p(x, y) = \phi_{\max} \exp\left(-2\frac{x^2}{w_{p,x}^2} - 2\frac{y^2}{w_{p,y}^2}\right)$$

with  $w_{p,x} = \frac{w_0}{\sqrt{p}}$  and  $w_{p,y} = \frac{w'_{0,y}}{\sqrt{p}} = \frac{w_0}{\sqrt{p}\sqrt{1+2\zeta^2}}$ . (20)

The effect on the circulating pulse (and limitation for the enhancement) can be described by the effective phase, which is the phase profile averaged over the intensity profile:

$$\begin{aligned} \phi_{\text{eff}} &= \iint \phi_p(x, y) I(x, y) dx dy / P \approx \phi_{\max} \frac{1}{1+p} \frac{2}{\sqrt{1+2\zeta^2}} \\ &= \phi_{\max} \frac{1}{1+p} \frac{P'}{P} \end{aligned} \quad (21)$$

and is with a very good approximation given by the factor  $1/(1+p)$ , which holds for a Gaussian beam, and the effective power fraction in the central fringe  $P'/P$ . The additional interference fringes do not contribute to the phase profile due to their smaller intensity, therefore reducing the effective phase. The effective phase limits the enhancement due to the blueshift of the circulating spectrum with respect to the impinging spectrum, which goes along with the ionization of the gas target [32,33]. This effect is known as ‘‘intensity clamping’’ and limits the (effective) phase to values  $\phi_{\text{eff}} < 6.3/F$  depending on the resonator finesse  $F$  [34].

The loss factor  $A$  due to spatial aberration of the phase profile can be estimated as the spatial overlap of the field with and without the aberrated phase [23]. For small phase aberrations, the overlap integral is given by the rms phase deviation  $\Delta\Phi$  (weighted with the intensity profile), and  $A$  reads as follows:

$$\begin{aligned} A &\approx 1 - \Delta\Phi^2 \\ &= 1 - \iint \mathcal{E}_{\text{NC}}^2(x, y) [\phi_p(x, y) - \phi_{\text{eff}}]^2 dx dy / P \\ &\approx 1 - \phi_{\text{eff}}^2 \left[ \frac{(1+p)^2}{(1+2p)} \frac{\sqrt{1+2\zeta^2}}{2} - 1 \right]. \end{aligned} \quad (22)$$

For the analytical evaluation, the field  $\mathcal{E}_{\text{NC}}$  has been replaced with the field of the central-fringe beam  $\mathcal{E}'$  [see Eq. (8)], which does not noticeably change the result as the phase profile  $\phi_p$  is zero outside the central fringe. The phase profile mainly represents a phase aberration. There is also a defocusing effect attributed to it, which is not subtracted in this evaluation. Moreover, only the end of the pulse sees the maximal phase  $\phi_{\max}$ . Both effects would yield a somewhat smaller value of  $\Delta\Phi^2$  when considered in the evaluation and therefore the loss caused by the plasma phase aberration is overestimated. The evaluation only provides an estimation for the loss, as it depends on many details (including the Gouy parameter, apertures, and additional aberrations in the resonator), whether the nonoverlapping part is completely lost at a resonator round trip and how the resonator possibly adapts the circulating field profile. The corresponding expression for

a Gaussian beam (also without removing a suitable defocusing) is:

$$A \approx 1 - \Delta\Phi^2 = 1 - \phi_{\text{eff}}^2 \left[ \frac{(1+p)^2}{(1+2p)} - 1 \right]. \quad (23)$$

The loss for a given effective phase is smaller for the Gaussian beam, e.g.,  $l = 2.8\%$  compared to  $5.2\%$  for the noncollinear beams, assuming  $p = 6$ ,  $\zeta = 2.2$  and an effective phase  $\phi_{\text{eff}} = 0.1$  rad.

The plasma formation goes along with absorption, which is proportional to the plasma phase and is typically small compared to other losses. Notably, however, the loss due to the aberration of the phase profile scales quadratically with the plasma phase. These relations represent a limitation to the strategy of lowering the enhancement and finesse (at accordingly larger impinging power) to allow a larger plasma phase, i.e., larger intensity and harmonic yield, with an acceptable intensity clamping:

If the resonator loss is dominated by the aberration from the plasma phase, its loss factor is  $A = 1 - c_1 \phi_{\text{eff}}^2$  with a coefficient  $c_1$  according to, e.g., Eqs. (22) or (23). If this resonator is operated at the clamping limit, the effective plasma phase is  $\phi_{\text{eff}} = \phi_{\text{lim}} \pi / F$ , where  $\phi_{\text{lim}}$  describes the limited plasma phase accumulated over the build-up time of the resonator  $\tau_{\text{bu}} = \frac{F}{\pi \nu_{\text{FSR}}}$ . In this situation the loss factor is related to the finesse by the following equation:

$$A = 1 - c_1 \frac{\phi_{\text{lim}}^2 \pi^2}{F^2}. \quad (24)$$

To achieve the largest enhancement at this design point of the resonator, it should be chosen impedance-matched ( $\bar{R}_{\text{IC}} = A$ ) for this loss factor, which corresponds to a finesse [compare Eq. (5)]:

$$F = 2\pi A / (1 - A^2). \quad (25)$$

Combining Eqs. (24) and (25) yields a loss factor  $A \approx 1 - \frac{1}{c_1 \phi_{\text{lim}}^2}$  and finesse  $F \approx \pi c_1 \phi_{\text{lim}}^2$  for the resonator limited by the plasma-phase aberrations and operated at the clamping limit. The corresponding finesse of the resonator without the plasma is  $F_0 \approx 2\pi c_1 \phi_{\text{lim}}^2$ , if it is assumed lossless (apart from the plasma-phase aberration), or somewhat smaller depending on the additional loss.

With  $c_1 = 5.2$  for  $p = 6$ ,  $\zeta = 2.2$  according to Eq. (22), and with  $\phi_{\text{lim}} = 6.3/\pi$  [34], this consideration yields  $F \approx 66$  (and  $\phi_{\text{eff}} = 0.1$  rad), which corresponds to  $F_0 \approx 131$  for the (lossless) resonator without plasma ( $\bar{R}_{\text{IC}} = 0.952$ ). This rough estimation can be considered a minimal finesse for a noncollinear resonator at the clamping limit and is close to the values used in our setups (see Sec. III).

Part of the loss due to the plasma aberration will be leakage through the slit in the mirror behind the HHG focus. A large power leaking through the slit affords suitable power-capable elements for separation of the harmonics. In the assessment of a suitable slit width for a noncollinear resonator, which should yield a large output-coupling efficiency for the harmonics and at the same time small loss for the circulating radiation, it should be considered, that this loss is not only given by the clipping of the unperturbed beam (at small intensity) but also

by the plasma aberration (at high intensity) and can therefore not be arbitrarily small.

In order to evaluate the power leaking through the slit, the beam profile in the far field of the focal plane, i.e., on the slit mirror, is considered. The field  $\mathcal{E}$  in the focal plane including the aberrated phase is

$$\begin{aligned}\mathcal{E}(x, y) &= \mathcal{E}_{\text{NC}}(x, y) \exp(i\phi_p(x, y)) \\ &\approx \mathcal{E}_{\text{NC}}(x, y) + i\mathcal{E}_{\text{NC}}(x, y)\phi_p(x, y) \\ &\approx \mathcal{E}_{\text{NC}}(x, y) + i\mathcal{E}'(x, y)\phi_p(x, y) \\ &\equiv \mathcal{E}_{\text{NC}}(x, y) + i\mathcal{E}_{\text{per}}(x, y).\end{aligned}\quad (26)$$

Here the phase term has been expanded and terms  $\sim O(\phi_p^2)$  neglected, yielding a sum of the unperturbed field  $\mathcal{E}_{\text{NC}}$  and a field  $\mathcal{E}_{\text{per}}$  describing the perturbation. In the perturbation, the field  $\mathcal{E}_{\text{NC}}$  is approximated by the field of the central-fringe beam  $\mathcal{E}'$ . The phase aberration takes shape in the far field. Here the perturbation corresponds to a beam profile with a large beam radius, stretching further out than the two beams of the unperturbed field, and with an on-axis contribution, which yields the leakage through the slit. The beam radii of the perturbation (intensity profile  $\sim \mathcal{E}'^2\phi_p^2$ ) in the focus are smaller than the focus radius  $w_0$ :

$$\frac{w_{\text{per},x}}{w_0} = \frac{1}{\sqrt{1+2p}} \quad \text{and} \quad \frac{w_{\text{per},y}}{w_0} = \frac{1}{\sqrt{1+2p}\sqrt{1+2\zeta^2}}, \quad (27)$$

and in the far field they are accordingly larger than the beam radius by that factor (e.g., factor 3.6 and 11.8 for  $p = 6$ ,  $\zeta = 2.2$ ). The effective power in this field describing the perturbation is [as an auxiliary quantity for the evaluation, using the on-axis intensity in the focus  $I_0$ ; see Eq. (11)]

$$P_{\text{per}} = I_0\phi_{\text{max}}^2 \frac{\pi w_{\text{per},x} w_{\text{per},y}}{2} = \frac{P\phi_{\text{eff}}^2(1+p)^2\sqrt{1+2\zeta^2}}{2(1+2p)}. \quad (28)$$

In the far field (with beam radius  $w$ ) the on-axis intensity of this field is

$$I_{\text{per}} = \frac{2P_{\text{per}}}{\pi w^2} \frac{1}{(1+2p)\sqrt{1+2\zeta^2}} = \phi_{\text{eff}}^2 \frac{(1+p)}{(1+2p)^2} \frac{P}{\pi w^2}. \quad (29)$$

Integrating in  $x$  direction and assuming a constant intensity across the slit width ( $y$  direction) yields the power leaking through a slit of width  $2b$ :

$$\begin{aligned}\frac{P_{\text{leak}}}{P} &= \phi_{\text{eff}}^2 \frac{(1+p)^2}{(1+2p)^{3/2}} \sqrt{\frac{2}{\pi}} \frac{b}{w} \\ &= \phi_{\text{eff}}^2 \frac{(1+p)^2}{(1+2p)^{3/2}} \sqrt{\frac{2}{\pi}} (\zeta - \sigma_{\text{slit}}).\end{aligned}\quad (30)$$

The intensity distributions on the slit mirror with and without the phase aberration from the plasma in the focus are shown in Fig. 9.

### F. Elliptical resonator mode

Elliptical beams can help to reduce cumulative plasma effects during resonator-assisted HHG. One speaks of a cumulative plasma, when the interaction volume after a laser pulse is not completely cleared before the next pulse arrives, which can cause, e.g., lock instabilities [33]. Using an elliptical resonator mode shortens the width of the interaction volume that

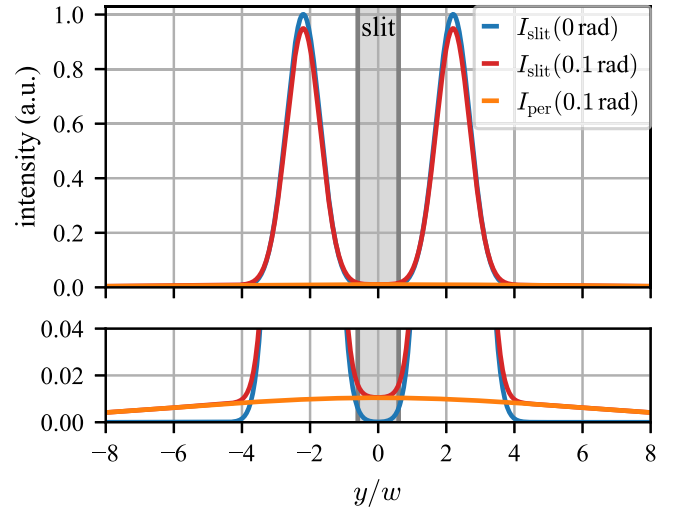


FIG. 9. The upper panel shows the intensity distribution on the slit mirror of the circulating beams without plasma (blue,  $\phi_{\text{eff}} = 0.1$  rad) and with plasma (red,  $\phi_{\text{eff}} = 0.1$  rad) for  $\zeta = 2.2$ ,  $\sigma_{\text{slit}} = 1.6$  and  $p = 6$ . For illustration also the intensity distribution of the field originating from the plasma aberration is shown (orange). The lower panel is the same plot with a scaled intensity axis.

the atoms have to traverse as depicted in Fig. 10 exemplary for a noncollinear resonator. Elliptical beams can be obtained in the resonator by introducing cylindrical mirrors, as will be discussed in detail below.

We call  $\varepsilon'$  the ellipticity of the central interference fringe and  $\varepsilon$  the ellipticity of the beam, defined in the following way:

$$\begin{aligned}\varepsilon' &= \frac{w_{0,x}}{w_{0,y}} = \frac{w_{0,x}}{w_{0,y}} \sqrt{1+2\zeta^2} = \frac{1}{\varepsilon} \sqrt{1+2\zeta^2} \\ \text{with } \varepsilon &= \frac{w_{0,y}}{w_{0,x}} \approx \frac{w_{\text{slit},x}}{w_{\text{slit},y}}.\end{aligned}\quad (31)$$

For a stigmatic beam, it is  $\varepsilon' > 1$ , i.e., the beam radius of the fringe is larger in the  $x$  direction. For an elliptic beam with  $\varepsilon > 1$ , the ellipticity of the central fringe can be made smaller, i.e., more round. For a noncollinear parameter  $\zeta = 2.2$  the required ellipticity to make the central fringe round is  $\varepsilon = 3.27$ , so even for the example in Fig. 10 with  $\varepsilon = 2.5$  an ellipticity of the central fringe of  $\varepsilon' = 1.3$  remains. Note that the ellipticity  $\varepsilon$  of the beam (assumed without astigmatism) also describes the ellipticity of the beam profile on the slit mirror (in the far field of the focus). In case of an elliptical beam, i.e., different far-field divergence angles in the transverse directions, the noncollinear parameter  $\zeta = \beta_{\text{NC}}/\vartheta_y$  is defined with respect to the far-field divergence angle in the direction of the displacement ( $y$  direction).

To quantify the cumulative plasma the authors of Ref. [35] have introduced a dimensionless parameter  $\xi_{\text{beam}}$ , which is the number of pulses an atom of the gas target “sees” while traversing the beam profile width (defined as FWHM, resulting in the factor  $\sqrt{2 \ln(2)}$  below) and is therefore a measure for the cumulative plasma. This parameter is calculated by

$$\xi_{\text{beam}} = \frac{\tau_{\text{beam}}}{\tau_{\text{rep}}} = \sqrt{2 \ln(2)} \frac{w_{0,x}}{v_{\text{gas}}} \nu_{\text{rep}}, \quad (32)$$

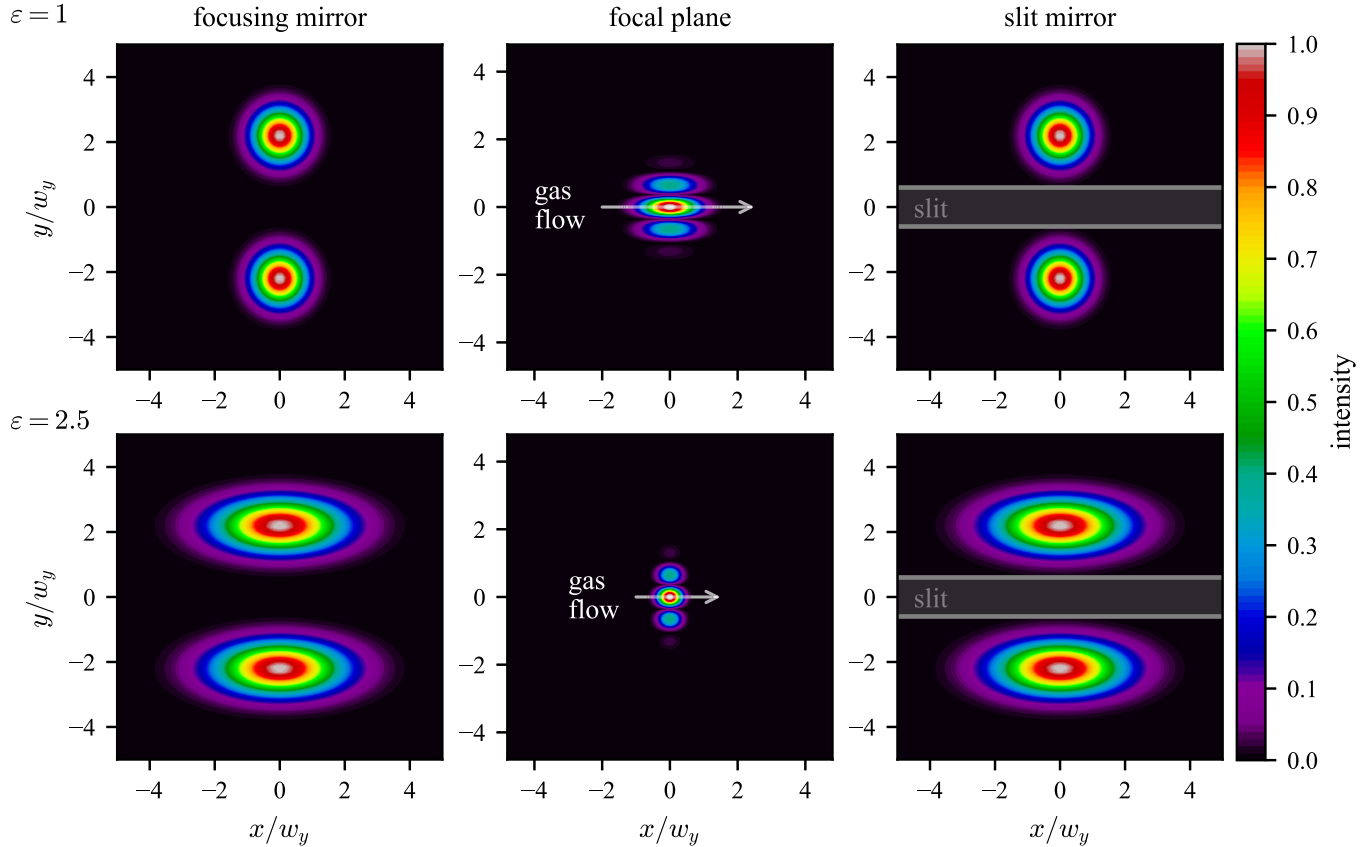


FIG. 10. Circulating beams on focusing mirror, focal plane and slit mirror for ellipticities  $\varepsilon = 1$  (upper row) and  $\varepsilon = 2.5$  (lower row), calculated with noncollinear parameter  $\zeta = 2.2$  and drawn in units of the respective beam size in the  $y$  direction. The white arrow in the focal plane indicates the gas flow direction for later HHG experiments: for larger  $\varepsilon$  the path for the gas atoms through the interaction volume becomes shorter which reduces cumulative plasma effects.

where  $\tau_{\text{beam}}$  is the time it takes for an atom to traverse the FWHM beam width,  $\nu_{\text{rep}}$  is the laser pulse repetition rate and  $\tau_{\text{rep}}$  its inverse,  $v_{\text{gas}}$  is the translational gas velocity,  $w_{0,x}$  is the beam waist radius in the  $x$  direction (direction of gas flow; see Fig. 10). This can be evaluated in terms of gas parameters and laser parameters using the following relations: The velocity of the gas flowing from the gas nozzle into the vacuum chamber of the HHG setup  $v_{\text{gas}} = \sqrt{5R_{\text{gas}}T_{\text{gas}}/M_{\text{gas}}}$  is given by the stagnation temperature  $T_{\text{gas}}$  of the monatomic gas (or gas mixture) and its (weighted-average) molar mass  $M_{\text{gas}}$ , where  $R_{\text{gas}}$  is the universal gas constant [36]. The focus radius  $w_{0,x} = \sqrt{\frac{4P}{\pi I_0 \varepsilon}}$  is related to the on-axis peak intensity  $I_0 = \frac{4P}{\pi w_{0,x} w_{0,y}}$ , peak power  $P$  and ellipticity  $\varepsilon = \frac{w_{0,y}}{w_{0,x}}$  of the noncollinear intensity profile. The peak power  $P = \frac{f_{\text{pulse}} P_m}{\nu_{\text{rep}} \tau}$  is related to the average power via the repetition rate, the pulse duration  $\tau_{\text{pulse}}$  and a pulse-shape factor  $f_{\text{pulse}}$ . If a fundamental mode instead of a noncollinear resonator is used, the intensity is  $I_0 = \frac{2P}{\pi w_{0,x} w_{0,y}}$ . This yields an expression that can be useful for design considerations:

$$\xi_{\text{beam}} = \sqrt{\frac{4 \ln(2)}{5\pi}} \left\{ \begin{array}{l} \sqrt{2} \\ 1 \end{array} \right\} \sqrt{\frac{f_{\text{pulse}} P_m \nu_{\text{rep}}}{I_0 \tau_{\text{pulse}}}} \sqrt{\frac{1}{\varepsilon}} \sqrt{\frac{M_{\text{gas}}}{R_{\text{gas}} T_{\text{gas}}}} \quad (33)$$

for  $\left\{ \begin{array}{l} \text{noncollinear geometry} \\ \text{fundamental mode} \end{array} \right.$

To avoid strong cumulative plasma effects the parameter should be limited to  $\xi_{\text{beam}} \lesssim 2$ ; each atom then sees two pulses while traversing the beam profile width and only about one pulse while traversing the somewhat smaller ion-generation volume (“single-pulse regime”); see Ref. [35] for details. The peak intensity is fixed within tight margin by the requirement of the HHG process (with a value depending on the gas species). It can be seen from Eq. (36) that cumulative effects represent a limitation for the scaling of the average power or for employing shorter pulses. Measures to reduce the cumulative plasma effects are speeding up the gas by reducing the (average) molar mass  $M_{\text{gas}}$  by mixing the heavy target gas with a light gas and by increasing  $T_{\text{gas}}$  with a heated gas nozzle [37], as well as increasing the time between the pulses, i.e., lowering the repetition rate  $\nu_{\text{rep}}$ . Note that the repetition rate contributes only with the square root, if the average power is kept constant, as the larger pulse energy and peak power requires a larger focus at fixed peak intensity. These three measures have been investigated and demonstrated to help limiting plasma effects and to increase HHG efficiency [35]. Reducing the focus radius in the direction of the gas flow by employing an elliptical focus is another possibility.

Note that  $\xi_{\text{beam}}$  is reduced linearly with the ellipticity of the resonator mode, if only the focus radius  $w_{0,x}$  in the direction of the gas flow is reduced (thereby increasing the focus intensity)

[see Eq. (32)], while it is reduced only with the square root of the ellipticity, if the focus radius in the other transverse directing is accordingly increased to keep the focus intensity constant; see Eq. (33).

For the noncollinear geometry three further advantages of an elliptical beam are first that the central fringe becomes rounder and therefore the produced harmonics as well. Second, the beam shape in the long arm makes better use of the round piezo mirror surface and third, as wedge mirrors with a given wedge angle restrict the resonator to be used at a certain position in the stability range, another advantage is that by changing the ellipticity one regains some flexibility in adjusting the focus intensity without having to change the wedge mirrors.

Generating an elliptical mode inside an enhancement resonator is possible by the presence of astigmatic elements, for instance simply the spherical mirrors which are hit under an angle  $\alpha$ . In a symmetric bow-tie resonator  $\alpha > 0$  results in an elliptical beam (and no astigmatism, due to the symmetry). To have a visible effect on the ellipticity, the angle of incidence  $\alpha$  on the spherical mirrors must be either large or the resonator must be operated close to the edge of the stability range. It is also possible to include cylindrical mirrors in an enhancement resonator to shape the circulating beam in only one transverse direction [38]. Cylindrical mirrors can be used to bring the resonator in the  $x$  direction close to the lower edge of the stability range, while leaving the  $y$  direction unchanged i.e., in the  $y$  direction the resonator is at the position in the stability range that yields the desired noncollinear parameter  $\zeta$  for a given wedge angle. In this situation, already small changes in the position in the stability range have a large effect on the ellipticity of the circulating beams while leaving  $\zeta$  almost unchanged.

For elliptical resonator modes without astigmatism the on-axis intensity along the propagation becomes

$$I(0, 0, z) = I_0 \frac{\exp\left(-2\zeta^2 \frac{z^2/z_{R,y}^2}{1+z^2/z_{R,y}^2}\right)}{\sqrt{(1+z^2/z_{R,x}^2)(1+z^2/z_{R,y}^2)}}, I_0 = \frac{4P}{\pi w_{0,x} w_{0y}} \quad (34)$$

with the Rayleigh lengths  $z_{R,x}$  and  $z_{R,y}$  in the  $x$  and  $y$  direction, respectively. The resonator only maintains its symmetry when one cylindrical mirror is placed in the middle of the long arm or two cylindrical mirrors with the same ROC are placed symmetrically around the middle of the long arm. A different position or different ROCs will additionally result in astigmatism. Like the design considerations on the positioning of the wedge mirror, for a bow-tie resonator it is easier to use two cylindrical mirrors to maintain the symmetry. Elliptical resonator modes require a corresponding mode matching of the impinging beam, which can be achieved with cylindrical lenses. Note that the ellipticity of the circulating mode's beam profile in the long arm is larger than on the focusing and slit mirrors. This should be considered for mode matching.

### III. LASER DESIGN TO SCALE HHG POWER

In the following we describe two setups at Fraunhofer ILT and at MPQ that are built for high-precision spectroscopy in

the VUV and EUV and scale HHG power with a low-finesse resonator. The two systems have a similar architecture: They consist of a high-power frequency comb (oscillator and high-power amplifier) followed by nonlinear pulse compression employing the multi-pass-cell spectral broadening (MPCSB) scheme [39], as shorter pulses yield a larger HHG conversion efficiency [40]. The relatively new MPCSB scheme plays a key role in power scaling of the HHG setup, as it overcomes the limitation by self-focusing which limits the pulse energy to  $< 1 \mu\text{J}$  from nonlinear spectral broadening in a solid-core fiber. The MPCSB scheme allows combining short pulses with pulse energies of a few  $\mu\text{J}$ , thereby exploiting the high average power of state-of-the-art femtosecond lasers at a repetition rate suitable for resonator-assisted HHG [41,42], which has been demonstrated in Ref. [6]. The HHG takes place inside a noncollinear enhancement resonator, consisting of highly reflective resonator mirrors featuring a high damage threshold and a small dispersion to support pulse durations down to  $\sim 50$  fs (coatings with even smaller dispersion are possible [43] at the cost of a reduced damage threshold).

Two pivotal optical elements of the enhancement resonator have been developed by Layertec: The first element is the wedge mirror with a defined wedge angle that features a small gap and small height difference or tilt between the two segments. The two segments of the wedge mirror are passively adjusted and optically contacted to a common base to achieve a small gap ( $< 100 \mu\text{m}$ ). Optical contacting is completely free of additives and formed without additional layers such as solder alloys or organic adhesives. It therefore helps to obtain the very small height difference between the two segments as well as the stability of the components position to each other during the lifetime of the assembly. Furthermore, it significantly reduces the effects of thermal expansion, hysteresis, or mechanical losses observed in adhesives or solders, and alleviates issues of outgassing and contamination of optical surfaces. Despite these benefits, optical contact bonds are of limited mechanical strength and susceptible to various mechanical and environmental loads, especially humidity, thermal and mechanical shock, and vibration. An additional ultrashort-pulse (USP) laser micro welding process (as described in Ref. [44]) overcomes these drawbacks of optical contacts while maintaining all its upsides. Laser micro welding significantly increases mechanical strength, robustness against environmental influences, and secures the optical contact bond against penetration of humidity. It preserves the adjustment state of the components with respect to each other as is achieved by optical contacting. The welding seam is very localized and generated with minimized thermal energy, thus limiting any effects on deformation of the optical surfaces and minimizing global stresses and deformation of the assembly. The localized processing enables the sequential construction of highly precise, multicomponent optical element such as the wedge mirror. The second element is the segmented input coupler, which is made from a single substrate and is coated by lithographic methods to have a sharp transition from the HR to the PR segment. Note that this sharp transition makes a small beam displacement on the input coupler possible, and therefore a small beam displacement at the position of the PZT mirror which can hence be small and light. As the PR segment of the input coupler has fewer layers than the HR segment,

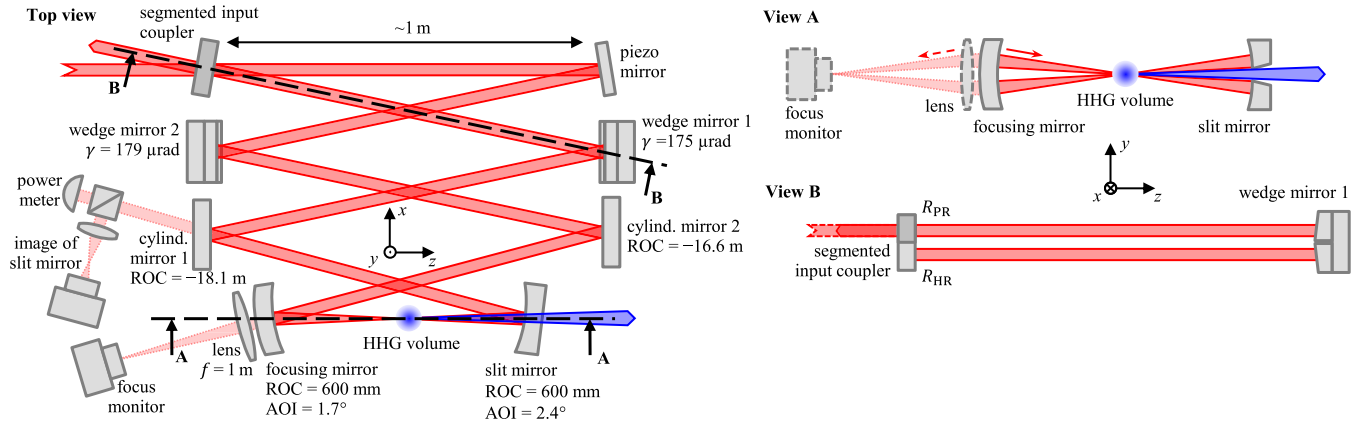


FIG. 11. Schematic representation of the noncollinear resonator at Fraunhofer ILT. The resonator consists of eight mirrors and the beam is displaced in the  $y$  direction. Two cylindrical mirrors make the circulating beams elliptical. The leakage through the focusing mirror is used to monitor the relative phase between the two circulating beams (focus monitor) and the leakage through cylindrical mirror 1 allows to image the slit mirror for resonator alignment and measurement of  $\zeta$ .

the PR is underfired with a fused-silica layer to achieve a small phase difference upon reflection on the two segments. Pictures of an input coupler and a wedge mirror are shown in Fig. 14.

#### A. Layout of the HHG setup at Fraunhofer ILT

The laser system at Fraunhofer ILT is designed to generate a VUV frequency comb for performing spectroscopy on the Th-229 isomer and to build a nuclear clock within the “ThoriumNuclearClock” ERC Synergy Grant project [16]. The isomer transition wavelength is 148.38 nm which can be reached with high-harmonic generation (HHG) producing the 7th harmonic of 1039 nm. Laser spectroscopy on the isomer in Th-229-doped crystals has already been successfully performed with pulsed nanosecond VUV lasers based on four-wave mixing [45,46] and with a VUV frequency comb [47].

The laser oscillator is a commercial low-noise frequency comb with a repetition rate of 80 MHz centered at 1050 nm. The repetition rate is reduced to 40 MHz with a pulse picker and the frequency comb will be amplified to 200 W average power with a commercial Yb: fiber amplifier, followed by a two-stage MPCSB setup to compress the pulses down to 50 fs. The resonator finesse is  $F = 102$ , while the impinging power after pulse compression and the residual beam path is expected to be about 180 W.

The repetition rate of 40 MHz necessitates a resonator length of 7.5 m. Using eight resonator mirrors results in a reasonable resonator size with about 1 m mirror distance. At the same time, at least eight mirrors are needed to include all the functionalities needed for the noncollinear resonator: input coupler, PZT mirror, two wedge mirrors, two cylindrical mirrors, focusing mirror and slit mirror. We confirmed with a frequency comb centered at 1040 nm, that the resonator supports an optical bandwidth of 70 nm. The schematics of the resonator design are shown in Fig. 11 and the relevant resonator characteristics calculated with the ABCD matrix formalism are listed in Table I. This resonator design corresponds to the situation shown in Fig. 6(b), with similar relative beam displacements  $\delta$  on the resonator mirrors. Xenon serves

as gas target for HHG and requires intensities of about  $8 \times 10^{13} \text{ W/cm}^2$  in the focus. Using an input coupler with  $R_{\text{PR}} = 90\%$  and assuming a realistic loss  $l = 0.9\%$  and a spectral and spatial overlap  $U = 77\%$  (without reduced overlap due to intensity clamping) the enhancement of the resonator is  $E = 43$ . Operated at full impinging power and with intensity clamping we expect to reach on-axis intensities of up to  $I_0 = 5 \times 10^{13} \text{ W/cm}^2$  to  $15 \times 10^{13} \text{ W/cm}^2$  for ellipticities  $\varepsilon = 1$  to  $\varepsilon = 3$ , respectively (calculated with an energy fraction contained in the main pulse of 0.7, an enhancement reduction factor due to intensity clamping of 0.65, an impinging power of 180 W and central-fringe radii  $w_{0,x} = 67 \mu\text{m} / \varepsilon$  and  $w'_{0,y} = 20 \mu\text{m}$ ).

For the operation point of our design with an ellipticity  $\varepsilon = 2.54$  (Table I), the parameter describing the cumulative plasma effects is  $\xi_{\text{beam}} = 1.9$  according to Eq. (32), assuming a gas velocity of  $v_{\text{gas}} = 648 \text{ m/s}$ , which is reached for a gas mixture He:Xe of 4:1 at 300 K [35]. This is within the single-pulse regime, and small cumulative plasma effects are expected (see Sec. II F).

#### B. Layout of the HHG setup at MPQ

The HHG system at the MPQ in Garching has a very similar architecture. The purpose of this laser system is to generate an EUV frequency comb with a central wavelength of 60.8 nm for the excitation of the  $1s-2s$  transition in  $\text{He}^+$  [15]. The spectroscopy will serve as a precise test of QED, which describes simple atomic systems. Resonator-assisted HHG is driven by an ultrastable high-power frequency comb to access the 17th harmonic of the fundamental laser. The details of the system are presented in [14] and will be briefly described here. The laser system is seeded by a home-built ytterbium-doped potassium yttrium tungstate (Yb:KYW) mode-locked oscillator with a repetition rate of 40 MHz, a central wavelength of 1030 nm and an averaged output power of 10 mW. After pre-amplification in a two-stage solid-state amplifier, the average power is raised to 2.7 W, which is sufficient to seed a high-power Innoslab amplifier that provides near 260 W output power [48]. After a two-stage MPCSB

TABLE I. Calculated beam displacement  $y_c$ , beam radii  $w_x$ ,  $w_y$ , and corresponding relative beam displacement  $\delta = y_c/w_y$  on the resonator mirrors and additional parameters at the planned operation point of the noncollinear resonator at ILT. The focus displacement is the distance of the beam intersection to the beam waist position in the  $x$  direction. Both, focus displacement and astigmatism are given relative to the Rayleigh length in the  $x$  direction  $z_{R,x}$  (i.e., relative to the smaller value).

	$y_c$	$w_x \times w_y$	$\delta$
Slit mirror	3.5 mm	3.9 mm $\times$ 1.5 mm	2.25
Cylindrical mirror 1	3.2 mm	3.6 mm $\times$ 1.4 mm	2.24
Wedge mirror 1	2.8 mm	3.6 mm $\times$ 1.3 mm	2.16
Segmented IC	2.8 mm	3.6 mm $\times$ 1.2 mm	2.27
PZT mirror	2.8 mm	3.5 mm $\times$ 1.2 mm	2.27
Wedge mirror 2	2.8 mm	3.6 mm $\times$ 1.3 mm	2.16
Cylindrical mirror 2	3.1 mm	3.5 mm $\times$ 1.4 mm	2.24
Focusing mirror	3.5 mm	3.9 mm $\times$ 1.5 mm	2.24
Noncollinear angle $\beta_{NC}$		1.28 $^\circ$	
Noncollinear parameter $\zeta$		2.25	
Central fringe radii $w_{0,x} \times w'_{0,y}$		26 $\mu\text{m} \times 20 \mu\text{m}$	
Resonator short-arm length $d$		620.4 mm	
Gouy parameter $\psi_{E,x}, \psi_{E,y}$		1.05 $\pi$ , 1.39 $\pi$	
Ellipticity $\varepsilon$ (of the focus)		2.54	
Astigmatism $\frac{z_{0,y} - z_{0,x}}{z_{R,x}}$		0.03	
Focus displacement $\frac{z_{\text{intersection}} - z_{0,x}}{z_{R,x}}$		-0.14	
Slit width $2b$		2.0 mm	
Safety distance at slit $\sigma_{\text{slit}}$		1.60	

setup and additional spectral filtering to tune the central wavelength to 1033 nm, the remaining average power is about 200 W. Due to the residual chromatic dispersion and the structured spectrum from the nonlinear spectral broadening process, the pulses consist of a 68-fs main pulse and a broader pedestal. The main peak contains about 70% of the pulse energy and a peak power of 32 MW is reached.

The frequency comb is phase-stabilized by locking a comb mode to an ultra-stable continuous-wave (cw) laser at 1033 nm. This wavelength corresponds to the 17th subharmonic of 60.8 nm, the wavelength used to drive the  $1s$ - $2s$  two-photon transition. The high bandwidth and long-term stable stabilization are achieved by controlling both the resonator length of the oscillator and the driving frequency of an acousto-optic modulator (AOM) placed at its output. Additionally, the heterodyne beat-note between the comb and the cw reference laser is obtained right before the enhancement resonator and feedback is given to a second AOM placed before the Innoslab amplifier, where the power level is acceptable for the AOM. In this way, phase-noise introduced during the long optical path from the seed to the HHG resonator is precompensated [14]. The carrier-envelope offset frequency of the comb does not need to be stabilized for performing direct-comb spectroscopy on the  $1s$ - $2s$  two-photon transition of  $\text{He}^+$ , due to the inherent noise-cancellation on the modes symmetrically displaced from the mode on-resonance [15].

Our 7.49-m ring resonator for HHG is folded into 16 mirrors to fit into a 40 cm  $\times$  80 cm vacuum chamber (see Fig. 12). Same as in the setup at ILT, the resonator comprises a segmented input coupler, a PZT mirror for stabilizing the resonator length, two wedge mirrors, a focusing mirror and a slit mirror for output-coupling the harmonics. The wedge angle of the wedge mirrors is 270  $\mu\text{rad}$ . The slit has a width of  $2b = 0.3$  mm and was produced by inverse laser drilling [49].

The radius of curvature is 500 mm for the focusing mirror and 300 mm for the slit mirror. This creates an asymmetry of the resonator that displaces the intersection plane and the focal plane from the middle of the short arm. This asymmetric configuration was chosen to obtain suitable focal size with the focusing mirrors that were available at the time. To fit the beams onto the PZT mirror with a smaller diameter of  $1/2''$  and to avoid clipping on other optical elements, the

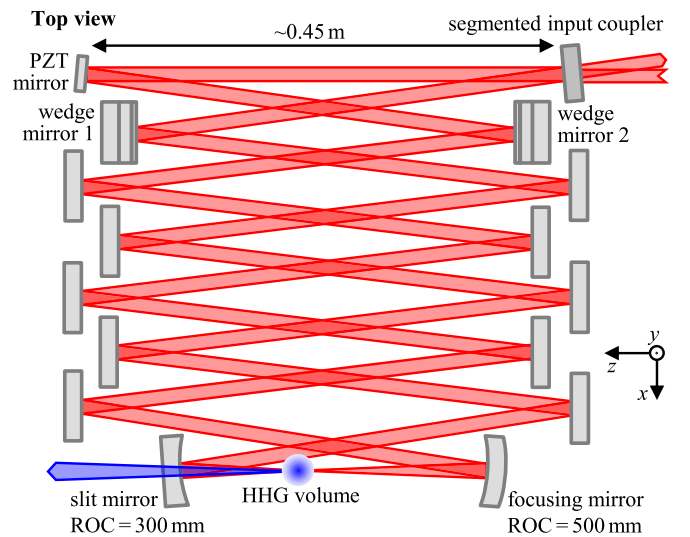


FIG. 12. Schematic representation (top view) of the noncollinear resonator at MPQ. The resonator consists of 16 mirrors which is necessary to fit it into the vacuum chamber. The noncollinear beams are displaced in the  $y$  direction (perpendicular to the resonator plane), which allows fitting the two beams through the gap in the first row of mirrors on each side.

TABLE II. Calculated displacement  $y_c$ , beam radius  $w$  and corresponding relative beam displacement  $\delta = y_c/w$  on the most relevant mirrors and additional parameters of the noncollinear HHG resonator at MPQ.

	$y_c$	$w$	$\delta$
Slit mirror	2.75 mm	1.18 mm	2.33
Wedge mirror 1	2.01 mm	1.00 mm	2.02
Segmented IC	2.14 mm	1.06 mm	2.03
PZT mirror	2.28 mm	1.13 mm	2.21
Wedge mirror 2	2.40 mm	1.23 mm	1.96
Focusing mirror	4.72 mm	1.99 mm	2.37
Noncollinear angle $\beta_{\text{NC}}$		1.03 °	
Noncollinear parameter $\zeta$		2.36	
Central fringe radii $w_{0,x} \times w'_{0,y}$		43 $\mu\text{m} \times 12 \mu\text{m}$	
Resonator short-arm length $d$		413.5 mm	
Gouy parameter $\psi_E$		1.52 $\pi$	
Focus displacement $\frac{z_{\text{intersection}} - z_{R,x}}{z_{R,x}}$		0.28	
Slit width $2b$		0.3 mm	
Safety distance at slit $\sigma_{\text{slit}}$		2.20	

MPQ resonator, unlike the ILT setup, does not use cylindrical mirrors and therefore does not employ an elliptical mode. With an input coupler with  $R_{\text{PR}} = 88\%$  and losses per round trip  $l < 0.2\%$ , the resonator has an enhancement of  $E = 39$  and a coupling of 65%. Up to 5.5 kW of circulating power (adding up the two circulating pulses) and on-axis intensity  $I_0 = 6 \times 10^{13} \text{ W/cm}^2$  is achieved in the resonator, when the impinging power is about 140 W. Higher impinging power resulted in a stronger thermal drift and locking instability due to nonlinear plasma effects. Roughly 10  $\mu\text{W}$  of average power per harmonic order are outcoupled from the resonator at wavelengths around 60.8 nm. Relevant geometrical parameters calculated via the ABCD matrix formalism (neglecting the small angle of incidence on the curved mirrors) are shown in Table II.

We currently use pure xenon for the HHG target which yields a translational gas velocity of  $v_{\text{gas}} = 305 \text{ m/s}$  and a parameter describing the cumulative plasma effects of  $\xi_{\text{beam}} = 6.6$  [Eq. (32)]. We can decrease cumulative plasma effects and potentially increase the harmonic power by admixing helium at the cost of a higher gas load and xenon consumption. We expect to reach the single-pulse regime for a gas mixture He:Xe of 9:1, bringing the parameter to  $\xi_{\text{beam}} = 2.3$ .

#### IV. CHARACTERIZATION OF A NONCOLLINEAR ENHANCEMENT RESONATOR WITH WEDGE MIRRORS

This section presents a thorough characterization of a noncollinear enhancement resonator and of the individual optical components. The following experiments demonstrate a noncollinear enhancement resonator with small round-trip loss, achieving the desired enhancement at the desired noncollinear parameter  $\zeta$  and ellipticity on the slit mirror  $\varepsilon$ . They are intended to highlight the physical relationships, functionality and versatility of a noncollinear enhancement resonator employing wedge mirrors. While HHG in an enhancement resonator employing wedge mirrors has been demonstrated

with the layout presented in Sec. III B [15], the experiments presented in this paper are conducted with a low-power continuous wave (cw) laser and without a gas target.

#### A. Experimental setup

The enhancement resonator used for the experiments is a slightly modified version of the system presented in Sec. III A and is schematically shown in Fig. 13. The resonator mirrors have been individually characterized, and some are shown in Fig. 14. An ECDL (external-cavity diode laser) cw laser with a wavelength of 1040 nm and an optical power of up to 50 mW is used for the characterization experiments. The resonator length is stabilized to the impinging laser with the Pound-Drever-Hall (PDH) technique. The output of the locking electronics is amplified and acts on the PZT mirror, which is a mirror glued onto a PZT tube [Fig. 14(e)]. In this setup one of the mirrors is a dedicated monitor mirror with a transmission of 0.6% to have a reasonable transmission signal despite the low cw laser power. The leakage beam through the focusing mirror, which uses a null-lens substrate, serves as focus monitor: The transmitted light is focused by a lens (focal length 1 m) placed directly behind the focusing mirror, which produces a focus of the two intersecting beams with the same shape and interference pattern as the focus inside the resonator, only larger by a factor 3.3 (given by the larger focal length compared to the reflection from the focusing mirror). From this interference pattern recorded with a camera one can infer the relative phase between the two circulating beams. Wedge mirror 2 is mounted on a PZT stage for translational movement in the  $y$  direction to control the relative phase between the two circulating beams. The focusing mirror is mounted on a translation stage to change the distance  $d$  between the curved mirrors and therefore the position in the stability range.

#### B. Enhancement of a noncollinear resonator mode

The two circulating beams must avoid the slit (slit mirror), the gaps (wedge mirrors), and the border between PR- and HR-segment (segmented input coupler) to minimize the loss in the noncollinear enhancement resonator. To ensure a good alignment between the resonator optics and the resonant modes, the transmitted (leakage) beams of various mirrors are used to image the surfaces of the alignment-sensitive mirrors onto several cameras. The time-averaged circulating power is determined by measuring the transmitted power through the monitor mirror with a photodiode power sensor. A photodetector (PD) (fast compared to the photodiode power sensor) monitors the resonator transmission signal. The ECDL used in the following experiments has phase fluctuations that lead to fast drops in the circulating power during the lock, which become more pronounced for the configurations with higher resonator finesse. As the relatively slow photodiode power sensor averages over these fast drops, the measured circulating power is multiplied by a factor  $f_c$  to get the circulating power in absence of these drops [22]. The factor  $f_c$  is calculated from the PD signal during the resonator lock as shown in Fig. 15. Later we confirmed with a low-noise laser that these drops were not due to the resonator-length lock and that the circulating power is stable to within 1.5% (peak-to-peak).

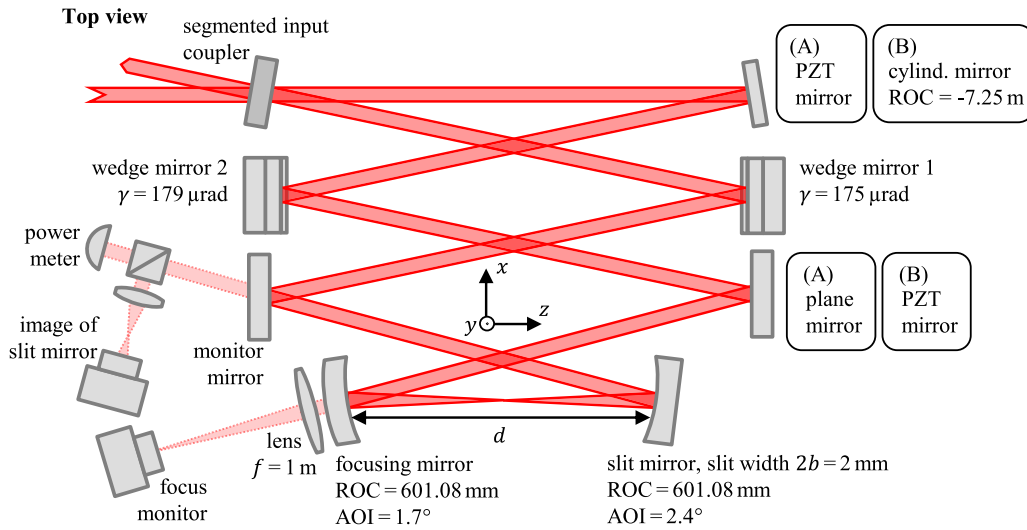


FIG. 13. Schematic drawing of the enhancement resonator (top view) in the two configurations that are used in the characterization experiments of this report (A and B). For the experiments with the cw laser the resonator length was  $L = 7.56 \text{ m}$ . The displayed values for the ROC of the cylindrical mirror and ROC of focusing and slit mirror give the best agreement with the experiment and are well within the tolerances given by the manufacturers. The focusing mirror’s substrate is a zero lens to keep the transmitted beam collimated. Inserting a lens in a flit mount in front of the focus-monitor camera (not shown) allows imaging wedge mirror 2. Furthermore, the segmented input coupler and wedge mirror 1 are imaged onto a third camera (not shown) through the transmission of the PZT mirror (A) and wedge mirror 1, respectively, to ease and check alignment.

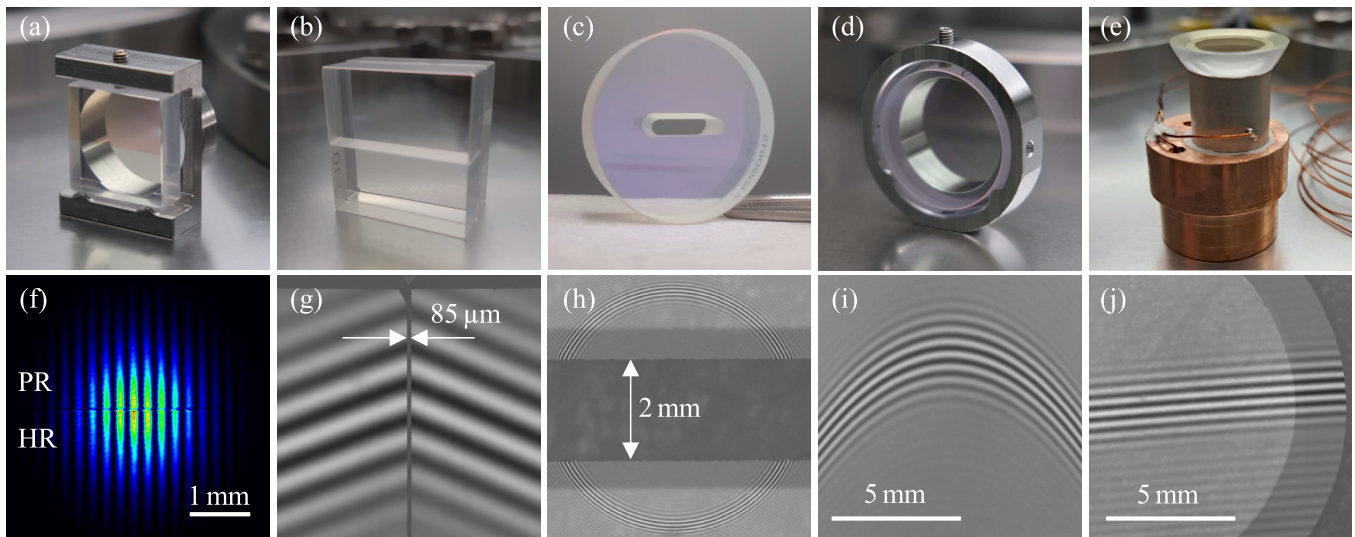


FIG. 14. Pictures of some of the resonator optics: (a) segmented input coupler ( $20 \times 20 \text{ mm}^2$ ), (b) wedge mirror ( $22 \times 22 \text{ mm}^2$ ), (c) slit mirror ( $\varnothing 25 \text{ mm}$ , ROC =  $601.08 \text{ mm}$ , slit drilled in the coated mirror by ultrasonic drilling), (d) cylindrical mirror ( $\varnothing 25.4 \text{ mm}$ , ROC =  $-7.25 \text{ m}$ ), (e) PZT mirror ( $\varnothing 19 \text{ mm}$ ). Below each picture is a respective characterization measurement: (f) interferogram of the input coupler, taken with a Michelson interferometer with a plane mirror as reference and a wavelength of  $1053 \text{ nm}$ . One can see the edge between PR and HR segment as horizontal line. The interference fringes on both segments are not shifted with respect to each other because the phase difference upon reflection is small. Additionally, we gold coated a second segmented IC of the same batch and ensured with a white light interferometer (WIM, model: Zygo NewView7300) that there is no height difference between the segments that could cause a phase shift of  $2\pi$  or multiples of  $2\pi$ . Pictures (g)–(j) show WIM measurements of the respective optics’ surfaces. One can see (g) the wedge angle from the slope of the fringes and that there is no height difference between the two segments of the wedge mirror, (h) that there is no distortion on the optical surface of the slit mirror even close to the slit and (j) that the edge of the PZT mirror is hardly deformed. (i) In contrast, the cylindrical mirror shows some surface deformation. All optics have been manufactured by Layertec, except for the cylindrical mirrors, which have been only coated by Layertec.

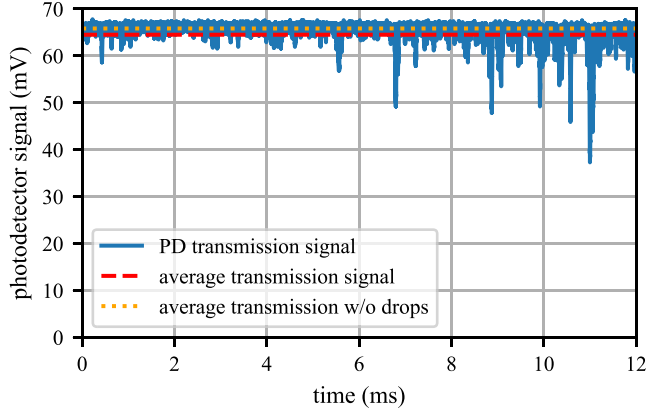


FIG. 15. Example of the photodetector (PD) transmission signal of the noncollinear resonator for an input-coupler reflectivity of  $R_{PR} = 0.92$ . The fast drops in the transmission signal are caused by phase fluctuations of the ECDL. The factor  $f_c$  is calculated as the ratio between average signal without drops (yellow dotted line) and the average signal (red dashed line).

The characterization results for various input couplers with different reflectivities  $R_{PR}$  are shown in Table III and in Fig. 16. We achieve an overlap of 90%, which is reasonable because approximately 5% of the impinging power are in the sidebands for PDH locking and another 3% reduction stems from imperfect mode matching as seen in higher transverse modes in the resonator length scan. The rest (2%) we attribute to the beam quality of the impinging beam plus a nonperfect spectral overlap. Furthermore, we achieve losses as low as 0.9%–1.0% including the 0.6% loss stemming from the monitor mirror.

### C. Variation of the noncollinear parameter

In a next step we measure the dependence of the noncollinear parameter  $\zeta$  on the position in the stability range. In the far field of the focus in the short resonator arm,  $\zeta$  can be read off from the relative beam displacement  $\delta$  of the two circulating beams. As the plane of the slit mirror is reasonably close to the far field and easily imaged through the monitor mirror,  $\zeta$  is measured as the relative beam displacement on the slit mirror  $\delta_{\text{slit}}$  by fitting two Gaussian functions to the

TABLE III. Measured coupling  $K$ , enhancement  $E$ , loss  $l$  (including 0.6% transmission-loss from the monitor mirror) and overlap  $U$  for 0 and  $\pi$  mode for four different reflectivities of the PR segment of the IC  $R_{PR}$ . The displayed values are the mean of five measurements at different impinging power. Furthermore, the table lists the correction factors  $f_c$  to calculate the circulating power.

$R_{PR}$	$f_c$	0 mode				$\pi$ mode			
		$K$	$E$	$l$	$U$	$K$	$E$	$l$	$U$
0.88	1.00	0.44	43	1.0%	90%	0.40	44	0.89%	89%
0.90	1.00	0.44	51	0.88%	90%	0.41	52	0.78%	90%
0.92	1.02	0.55	57	0.96%	91%	0.51	58	0.87%	90%
0.96	1.05	0.74	85	0.87%	90%	0.72	89	0.82%	91%

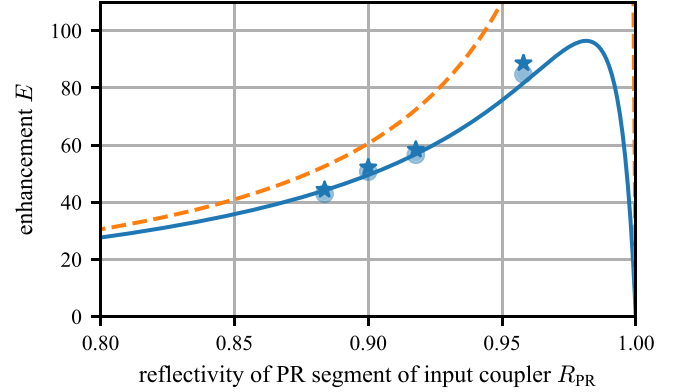


FIG. 16. Measured enhancement  $E$  for four different input couplers for 0 mode (circles) and  $\pi$  mode (stars) for  $\zeta = 2.25$ . The curves are the calculated enhancement for loss factors  $A = 0.991$  (blue, solid, as measured) and  $A = 0.997$  (orange, dashed, as expected when operating the resonator without a dedicated monitor mirror, thereby reducing the resonator loss by 0.6%), both for an overlap of  $U = 90\%$ .

intensity profile (integrated in the  $x$  direction), as shown in Fig. 17(c). The fit function  $I(y)$  allows for two different amplitudes  $I_{1,2}$  and centers  $y_{c,1/2}$  but uses only one value for the beam radius  $w_y$ :

$$I_1 \exp\left(-2 \frac{(y - y_{c,1})^2}{w_y^2}\right) + I_2 \exp\left(-2 \frac{(y - y_{c,2})^2}{w_y^2}\right). \quad (35)$$

The noncollinear parameter is determined from the fit by  $\zeta = |y_{c,1} - y_{c,2}|/2w_y$ . The values for  $\delta_{\text{wedge}2}$  are measured analogously from an image of wedge mirror 2. Another possibility is to infer  $\zeta$  from a fit on the focus profile measured on the focus monitor, but as the position of the focus monitor varies with the position in the stability range that would require a realignment of the camera position for each measurement, which is not practical. Furthermore, we compare the relative beam displacement at the second wedge mirror  $\delta_{\text{wedge}2}$  and the Gouy parameter  $\psi_E$  with our calculation. The Gouy parameter is read off from a resonator-length scan over the FSR and the position of the  $GH_{10}$  mode. The result is shown in Fig. 17 and the corresponding loss  $l$ , enhancement  $E$  and overlap  $U$  are plotted in Fig. 18 for different values of  $\zeta$ . The calculated curve for  $l$  (solid blue line in) is

$$l = T_{\text{monitor}} + \text{erfc}(\sqrt{2} \sigma_{\text{slit}}), \quad (36)$$

where  $T_{\text{monitor}}$  is the transmission through the monitor mirror and the second summand is twice the clipping loss of a Gaussian intensity profile at an edge with safety distance  $\sigma_{\text{slit}}$  (ratio of the distance from the beam to the edge of the slit and the beam radius). The factor of two accounts for the following propagation loss of the distorted beam [23].

For small values of  $\zeta$  we measure different loss factors for 0 and  $\pi$  mode which result from the interference of the two circulating beams: as illustrated in Fig. 19, in contrast to the 0 mode the intensity of the  $\pi$  mode vanishes on the resonator axis, which results in a smaller clipping loss and can be calculated similar to Eq. (36).

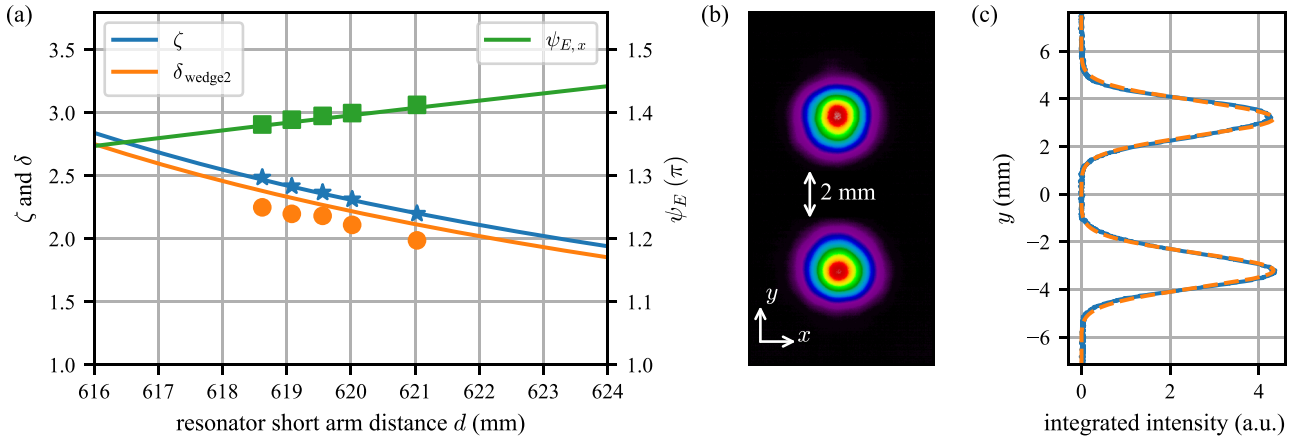


FIG. 17. (a) Comparison of the measured values of the  $\zeta$  (stars), the relative beam displacement on the second wedge mirror  $\delta_{\text{wedge2}}$  (circles) and the Gouy parameter in the  $x$  direction  $\psi_{E,x}$  (squares) for different positions in the stability range with the expected values from ABCD matrix calculation (solid lines). (b) Image of the slit mirror for  $\zeta = 2.2$ . The scale marks the position and width of the slit. (c) The noncollinear parameter  $\zeta$  is determined as the relative beam displacement.

**D. Relative phase of the noncollinear beams**

Although all resonator mirrors are monolithic, it is possible that the phase between the two circulating beams is not exactly 0 or  $\pi$  for several reasons: first, the IC mirror consists of two

segments with two different coatings and a different number of coating layers. The thinner PR coating (fewer layers) is underfired to compensate the phase difference upon reflection, but in general a small phase difference remains. Second, the wedge mirrors consist of two segments that are optically contacted onto a substrate and there can be a height difference between the two segments. Last, if the apex of the wedge mirrors is not exactly in the middle between the two circulating beams due to misalignment caused by, e.g., thermal drifts, the two beams acquire a phase difference. We take advantage of the last point and place one of the wedge mirrors (wedge mirror 2) on a PZT stage that allows moving the wedge mirror up and down ( $y$  direction) and thereby changing the relative phase between the two circulating beams (see Fig. 20). The expected change of the relative phase is  $\Delta\varphi = 2k\gamma\Delta y$ , where  $\gamma$  is the wedge angle,  $k$  is the wave number and  $\Delta y$  is the transverse

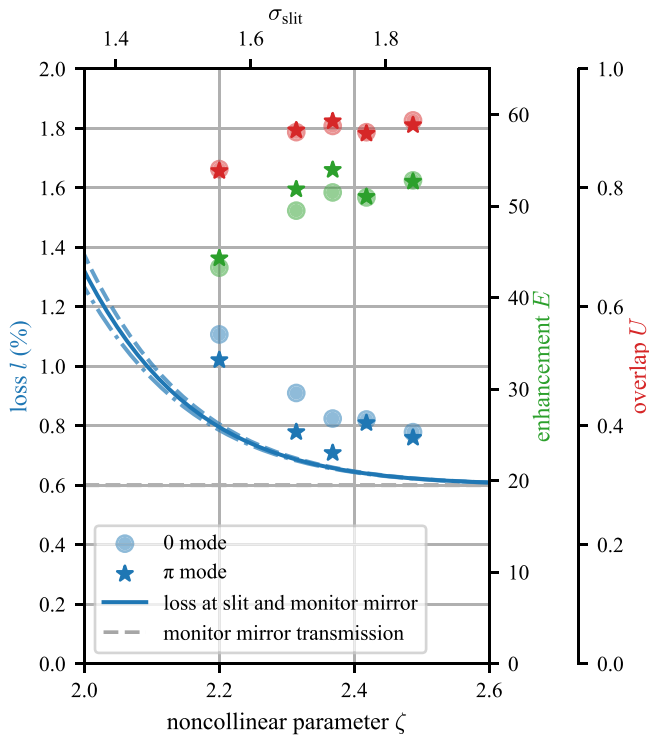


FIG. 18. Measured loss  $I$ , enhancement  $E$  and overlap  $U$  for different noncollinear parameters  $\zeta$ . The upper axis shows the corresponding safety distance  $\sigma_{\text{slit}}$  to the edge of the slit (slit width  $2b = 2.0$  mm). The solid blue line shows the calculated clipping loss of two Gaussian beams that do not interfere, the blue dashed and dash-dotted line show the loss for 0 and  $\pi$  mode and the gray dashed line indicates loss from the monitor mirror (transmission). For small  $\zeta$ , corresponding to small  $\sigma_{\text{slit}}$ , the clipping at the slit becomes larger.

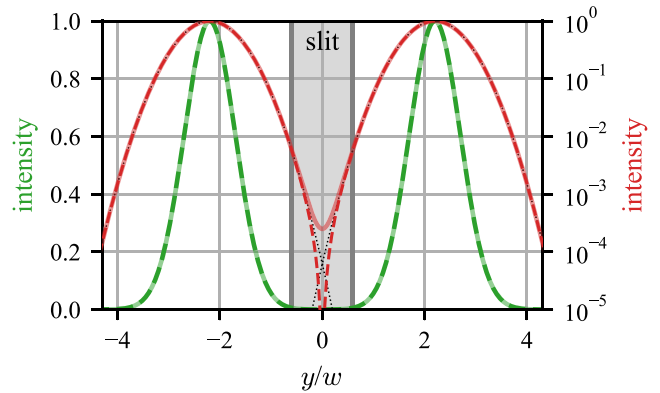


FIG. 19. Intensity distribution of two Gaussian beam profiles that are in phase (0 mode, solid) and  $180^\circ$  out of phase ( $\pi$  mode, dashed) on a linear (green) and a logarithmic scale (red) for  $\zeta = 2.2$  and  $\sigma_{\text{slit}} = 1.6$ . On the logarithmic scale it is clearly visible that the clipping loss at a slit (gray shaded area) is higher for the 0 mode compared to the  $\pi$  mode. The black dotted lines show the intensity distribution of two individual Gaussian beams.

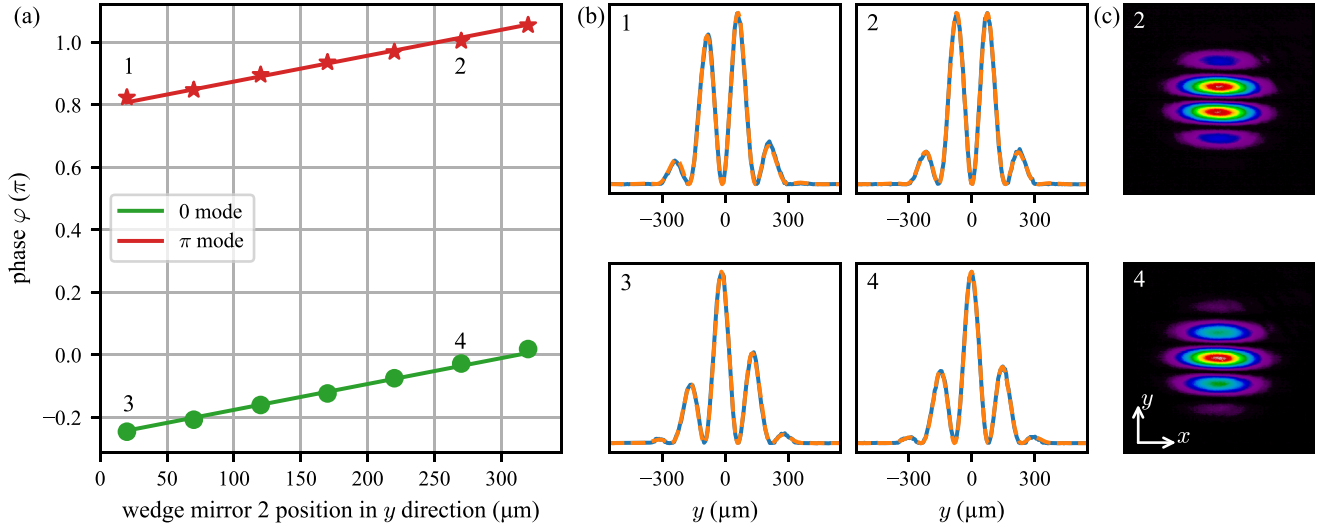


FIG. 20. The phase difference between the two circulating beams is controlled by displacing the wedge mirror in the  $y$  direction. Graph (a) shows the measured phase for 0 and  $\pi$  mode for several positions of the wedge mirror and a linear fit. Graphs (b) are four slices through the focus profile (solid blue, measured with focus monitor) with the fit (dashed orange) for determination of the phase difference, and the numbers indicate to which points the slices belong on graph (a). Points 2 and 4 correspond to  $\pi$  and 0 mode and the respective measured focus profiles are shown in panel (c).

displacement of the wedge mirror. The phase between the two beams is measured with the focus monitor, where the phase  $\varphi$  can be determined from fitting Eq. (7) (for  $x = 0$ ) to the intensity profile of the focus monitor, using  $P$ ,  $w_{0,y}$ ,  $\zeta$ , and  $\varphi$  as fit parameters. Once the  $y$ -position of the wedge mirror has been adjusted, the relative phase  $\varphi$  remained stable and did not have to be readjusted on a timescale of weeks.

### E. Elliptical mode with cylindrical resonator mirrors

For this experiment the enhancement resonator is changed to configuration (B) of Fig. 13 to include a cylindrical mirror and make the circulating beams elliptical. In configuration (B) the cylindrical mirror is placed close to the middle of the long arm to reduce astigmatism in the short arm while still using

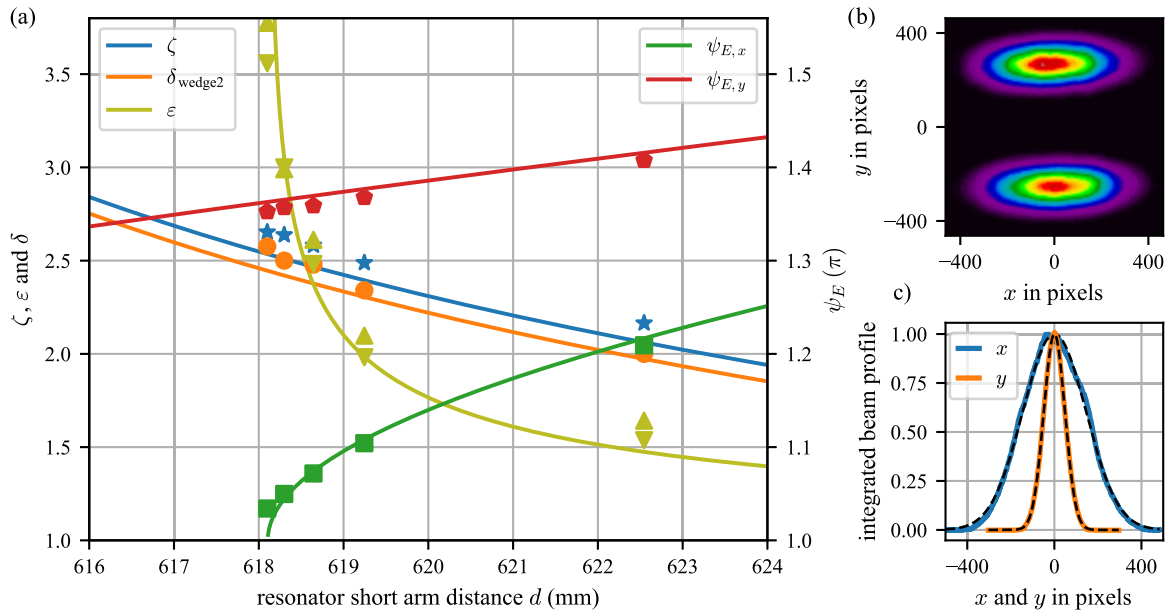


FIG. 21. (a) Experimentally measured ellipticity  $\epsilon$  (up facing triangles for upper beam, down facing triangles for lower beam) as a function of the position in the stability range and calculated curve (yellow line). Also depicted is the measured noncollinear parameter  $\zeta$  (stars) and relative beam separation  $\delta_{\text{wedge2}}$  on wedge mirror 2 (circles), as well as the Gouy parameter in the  $x$  direction  $\psi_x$  (squares) and in the  $y$  direction  $\psi_y$  (pentagon), together with the corresponding calculated curves. Ellipticity, noncollinear parameter and relative beam separation are evaluated from beam profiles of the corresponding planes imaged onto a camera. The Gouy parameters are evaluated from the position of transverse modes at a resonator scan. (b) Beam profile of the circulating mode on the slit mirror at  $\epsilon = 3$ . (c) Beam profile of the upper beam integrated in the  $x$  and  $y$  direction and Gaussian fits (black dashed curves), from which the ellipticity is calculated.

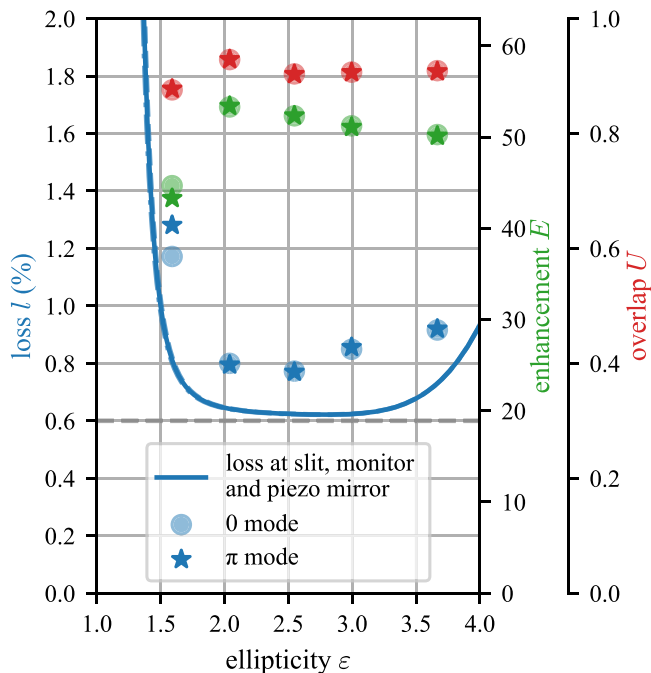


FIG. 22. Measured loss  $l$ , enhancement  $E$  and overlap  $U$  for different values of the ellipticity  $\varepsilon$ , which is adjusted via the position in the stability range. The solid blue line shows the calculated loss (including transmission loss at the monitor mirror and clipping loss at the slit and at the PZT mirror) of two Gaussian beams that do not interfere. Compared to Fig. 18, in this plot the difference between loss for 0 and  $\pi$  mode is hardly visible.

a dedicated monitor mirror, although that goes along with placing the PZT mirror at a position with a larger beam profile. A 1''-1''-adapter is used to mount the cylindrical mirror into a mirror mount to ease alignment of the cylindrical mirror axis [see Fig. 14(d)]. A precise alignment of this axis is crucial, as already small deviations of less than  $1^\circ$  lead to a visible transverse displacement of the circulating beams in the opposite  $x$  direction and hence a distorted focus profile. The ROC of the cylindrical mirror is chosen to bring the stability edge in the  $x$  direction (confocal stability edge  $\psi_{E,x} = \pi$ ) close to the desired position in the stability range in the  $y$  direction with the respective  $\zeta$ , so that already small changes of the resonator short-arm length have a large effect on the ellipticity. For the measurement we vary the resonator short-arm length again, and the results are shown in Fig. 21(a). To achieve a high spatial overlap, we use cylindrical lenses in a Galilean telescope to shape the impinging beam, with the focal lengths and distance adapted to the ellipticity of the circulating mode. The ellipticity is determined by fitting a Gaussian function to the beam profile on the slit mirror [see Fig. 21(c)];  $\zeta$ ,  $\delta$ , and  $\psi_E$  are determined as described in Sec. IV C.

Using cylindrical mirrors raises two concerns: First, their surface quality is typically worse compared to plane mirrors or spherical mirrors which potentially leads to additional losses in the enhancement resonator. Second, at one point the beam becomes so large in one direction that it does not fit any more on the PZT mirror, which is the smallest mirror in the

enhancement resonator. The measured loss, enhancement and overlap can be seen in Fig. 22. The increase in loss for an ellipticity of 1.5 results from the small  $\zeta$  at this position in the stability range and the corresponding clipping loss at the slit in the slit mirror. For large ellipticities it gets increasingly difficult to fit the beam onto the PZT mirror, but we achieve an enhancement  $E > 50$  for ellipticities up to  $\varepsilon = 3.7$ .

## V. SUMMARY

We developed and demonstrated a noncollinear resonator design for high-harmonic generation (HHG) by implementing specially developed optical elements: “wedge mirrors” and a segmented input coupler. In a noncollinear resonator, two beams circulate at the same time, intersect in the focal plane, and form an interference pattern. This interference pattern is dictated by the noncollinear parameter  $\zeta$  and the relative phase  $\varphi$  between the two circulating beams. For  $\varphi = 0$  (“0 mode”), the central fringe of the interference pattern can be used for HHG and while the generated harmonics propagate along the bisecting line and can leave the resonator through a slit in the collimating mirror, the circulating beams separate again and hit the collimating mirror avoiding the slit. The wedge mirrors consist of two plane segments which include a small angle to each other, and which are contact bonded onto a common substrate to form a monolithic element. Contrary to previous proposals and demonstrations, wedge mirrors eliminate the need to include separate mirrors for the two circulating beams in a noncollinear resonator. Therefore, a noncollinear resonator employing wedge mirrors features intrinsic pulse synchronization, reduces the alignment effort, and provides a possibility to monitor (and adjust) the relative phase  $\varphi$  between the two circulating beams. This noncollinear resonator design thereby overcomes the obstacles that have so far hampered taking full advantage of the benefits of noncollinear output-coupling of high harmonics: high output-coupling efficiency over a broad spectral range, no elements prone to degradation within the resonator, no angular dispersion of the harmonics, and low intensity at the edges of the slit in the output-coupling mirror.

This work provides a description of how resonator loss, enhancement and finesse can be understood in a noncollinear resonator geometry and gives layout considerations on how to set up a noncollinear enhancement resonator with wedge mirrors and a segmented input coupler. An estimation of output-coupling efficiency is given, along with a comparison to other output-coupling methods, as well as an estimation of the loss due to the phase aberration caused by ionization of the gas target. Two setups are presented, employing short pulses and low-finesse resonators to scale HHG efficiency. One system is operated at MPQ and one is under construction at Fraunhofer ILT.

Using a cw laser, a noncollinear enhancement resonator configuration was thoroughly characterized. The presented measurements demonstrate the physical relationships, functionality and versatility of a noncollinear enhancement resonator employing wedge mirrors and a segmented input coupler. We achieve low round-trip loss and the corresponding enhancement with four input couplers with different reflectivities of the partially reflecting segment. In the used

noncollinear resonator containing two wedge mirrors with a fixed wedge angle, the noncollinear parameter  $\zeta$  can be adjusted by changing the distance between the curved mirrors. We demonstrate fine tuning of the phase of the interference fringes in the focus by transversely moving one of the wedge mirrors. Once this phase is adjusted, it did not have to be readjusted on order of weeks. Employing cylindrical mirrors, ellipticities  $\varepsilon > 3$  of the circulating beams are achieved without compromising the resonator enhancement. Increasing the ellipticity makes the central interference fringe rounder and thereby decreases the distance in the direction of the gas flow of a HHG target. Therefore, elliptical beams offer a promising possibility to reduce cumulative plasma effects like locking instabilities in resonator-assisted HHG.

### ACKNOWLEDGMENTS

We thank Peter Rußbüldt and Christian Girr for fruitful discussions, Dominik Esser for drilling of slit mirrors, and

Wolfgang Simon and Rudolf Meyer for support at the mechanical design of the resonator setups.

We acknowledge support from the ERC Synergy Grant “ThoriumNuclearClock” (ID 856415), ERC Grant “XUV-COMB” (ID 742247), and Horizon 2020 nuClock (ID 664732). The research is part of the Munich Quantum Valley, which is supported by the Bavarian state government with funds from the Hightech Agenda Bayern Plus.

### DATA AVAILABILITY

The data that support the findings of this article are not publicly available upon publication because it is not technically feasible and/or the cost of preparing, depositing, and hosting the data would be prohibitive within the terms of this research project. The data are available from the authors upon reasonable request.

- 
- [1] D. C. Yost, T. R. Schibli, and J. Ye, Efficient output coupling of intracavity high-harmonic generation, *Opt. Lett.* **33**, 1099 (2008).
- [2] A. Ozawa, Z. Zhao, M. Kuwata-Gonokami, and Y. Kobayashi, High average power coherent VUV generation at 10 MHz repetition frequency by intracavity high harmonic generation, *Opt. Express* **23**, 15107 (2015).
- [3] See Supplementary Information for Ref. [35].
- [4] I. Pupeza, S. Holzberger, T. Eidam, H. Carstens, D. Esser, J. Weitenberg, P. Rußbüldt, J. Rauschenberger, J. Limpert, Th. Udem, A. Tünnermann, T. W. Hänsch, A. Apolonski, F. Krausz, and E. Fill, Compact high-repetition-rate source of coherent 100 eV radiation, *Nat. Photon.* **7**, 608 (2013).
- [5] M. Högner, T. Saule, and I. Pupeza, Efficiency of cavity-enhanced high harmonic generation with geometric output coupling, *J. Phys. B: At. Mol. Opt. Phys.* **52**, 075401 (2019).
- [6] T. Saule, S. Heinrich, J. Schötz, N. Lilienfein, M. Högner, O. deVries, M. Plötner, J. Weitenberg, D. Esser, J. Schulte, P. Russbüldt, J. Limpert, M. F. Kling, U. Kleineberg, and I. Pupeza, High-flux ultrafast extreme-ultraviolet photoemission spectroscopy at 18.4 MHz pulse repetition rate, *Nature Commun.* **10**, 458 (2019).
- [7] I. Pupeza, M. Högner, J. Weitenberg, S. Holzberger, D. Esser, T. Eidam, J. Limpert, A. Tünnermann, E. Fill, and V. S. Yakovlev, Cavity-enhanced high-harmonic generation with spatially tailored driving fields, *Phys. Rev. Lett.* **112**, 103902 (2014).
- [8] J. Weitenberg, P. Rußbüldt, T. Eidam, and I. Pupeza, Transverse mode tailoring in a quasi-imaging high-finesse femtosecond enhancement cavity, *Opt. Express* **19**, 9551 (2011).
- [9] C. Zhang, S. B. Schoun, C. M. Heyl, G. Porat, M. B. Gaarde, and J. Ye, Noncollinear enhancement cavity for record-high out-coupling efficiency of an extreme-UV frequency comb, *Phys. Rev. Lett.* **125**, 093902 (2020).
- [10] A. Cingöz, D. C. Yost, T. K. Allison, A. Ruehl, M. E. Fermann, I. Hartl, and J. Ye, Direct frequency comb spectroscopy in the extreme ultraviolet, *Nature* **482**, 68 (2012).
- [11] A. Ozawa and Y. Kobayashi, vuv frequency-comb spectroscopy of atomic xenon, *Phys. Rev. A* **87**, 022507 (2013).
- [12] C. Benko, T. K. Allison, A. Cingöz, L. Hua, F. Labaye, D. C. Yost, and J. Ye, Extreme ultraviolet radiation with coherence time greater than 1 s, *Nature Photon.* **8**, 530 (2014).
- [13] C. Zhang, P. Li, J. Jiang, L. von der Wense, J. F. Doyle, M. E. Fermann, and J. Ye, Tunable VUV frequency comb for  $^{229m}\text{Th}$  nuclear spectroscopy, *Opt. Lett.* **47**, 5591 (2022).
- [14] F. Schmid, J. Moreno, J. Weitenberg, P. Russbüldt, T. W. Hänsch, T. Udem, and A. Ozawa, An ultra-stable high-power optical frequency comb, *APL Photon.* **9**, 026105 (2024).
- [15] J. Moreno, F. Schmid, J. Weitenberg, S. G. Karshenboim, T. W. Hänsch, T. Udem, and A. Ozawa, Toward XUV frequency comb spectroscopy of the 1S-2S transition in  $\text{He}^+$ , *Eur. Phys. J. D* **77**, 67 (2023).
- [16] E. Peik, T. Schumm, M. S. Safronova, A. Pálffy, J. Weitenberg, and P. G. Thirolf, Nuclear clocks for testing fundamental physics, *Quantum Sci. Technol.* **6**, 034002 (2021).
- [17] I. Pupeza, C. Zhang, M. Högner, and J. Ye, Extreme-ultraviolet frequency combs for precision metrology and attosecond science, *Nature Photon.* **15**, 175 (2021).
- [18] C. Gohle, T. Udem, M. Herrmann, J. Rauschenberger, R. Holzwarth, H. A. Schuessler, F. Krausz, and T. W. Hänsch, A frequency comb in the extreme ultraviolet, *Nature* **436**, 234 (2005).
- [19] R. J. Jones, K. D. Moll, M. J. Thorpe, and J. Ye, Phase-coherent frequency combs in the vacuum ultraviolet via high-harmonic generation inside a femtosecond enhancement cavity, *Phys. Rev. Lett.* **94**, 193201 (2005).
- [20] K. D. Moll, R. J. Jones, and J. Ye, Output coupling methods for cavity-based high-harmonic generation, *Opt. Express* **14**, 8189 (2006).
- [21] A. Ozawa, A. Vernaleken, W. Schneider, I. Gotlibovych, Th. Udem, and T. W. Hänsch, Non-collinear high harmonic generation: A promising outcoupling method for cavity-assisted XUV generation, *Opt. Express* **16**, 6233 (2008).
- [22] M. Högner, T. Saule, S. Heinrich, N. Lilienfein, D. Esser, M. Trubetskov, V. Pervak, and I. Pupeza, Cavity-enhanced noncollinear high-harmonic generation, *Opt. Express* **27**, 19675 (2019).

- [23] J. Weitenberg, P. Rußbüldt, I. Pupeza, Th. Udem, H.-D. Hoffmann, and R. Poprawe, Geometrical on-axis access to high-finesse resonators by quasi-imaging: A theoretical description, *J. Opt.* **17**, 025609 (2015).
- [24] W. Nagourney, *Quantum Electronics for Atomic Physics and Telecommunication*, 2nd ed. (Oxford University Press, Oxford, 2014).
- [25] F. Zomer, Y. Fedala, N. Pavloff, V. Soskov, and A. Variola, Polarization-induced instabilities in external four-mirror Fabry-Perot cavities, *Appl. Opt.* **48**, 6651 (2009).
- [26] J. A. Arnaud and H. Kogelnik, Gaussian light beams with general astigmatism, *Appl. Opt.* **8**, 1687 (1969).
- [27] T. E. Gureyev, A. Roberts, and K. A. Nugent, Partially coherent fields, the transport-of-intensity equation, and phase uniqueness, *J. Opt. Soc. Am. A* **12**, 1942 (1995).
- [28] S. Gigan, L. Lopez, N. Treps, A. Maître, and C. Fabre, Image transmission through a stable paraxial cavity, *Phys. Rev. A* **72**, 023804 (2005).
- [29] O. Pronin, V. Pervak, E. Fill, J. Rauschenberger, F. Krausz, and A. Apolonski, Ultrabroadband efficient intracavity XUV output coupler, *Opt. Express* **19**, 10232 (2011).
- [30] Y.-Y. Yang, F. Süßmann, S. Zherebtsov, I. Pupeza, J. Kaster, D. Lehr, H.-J. Fuchs, E.-B. Kley, E. Fill, X.-M. Duan, Z.-S. Zhao, F. Krausz, S. L. Stebbings, and M. F. Kling, Optimization and characterization of a highly-efficient diffraction nanograting for MHz XUV pulses, *Opt. Express* **19**, 1954 (2011).
- [31] E. D. Palik, *Handbook of Optical Constants of Solids*, Vols. 1 and 2 (Academic Press, San Diego, 1998).
- [32] D. C. Yost, A. Cingöz, T. K. Allison, A. Ruehl, M. E. Fermann, I. Hartl, and J. Ye, Power optimization of XUV frequency combs for spectroscopy applications, *Opt. Express* **19**, 23483 (2011).
- [33] T. K. Allison, A. Cingöz, D. C. Yost, and J. Ye, Extreme nonlinear optics in a femtosecond enhancement cavity, *Phys. Rev. Lett.* **107**, 183903 (2011).
- [34] S. Holzberger, N. Lilienfein, H. Carstens, T. Saule, M. Högner, F. Lücking, M. Trubetskov, V. Pervak, T. Eidam, J. Limpert, A. Tünnermann, E. Fill, F. Krausz, and I. Pupeza, Femtosecond enhancement cavities in the nonlinear regime, *Phys. Rev. Lett.* **115**, 023902 (2015).
- [35] G. Porat, C. M. Heyl, S. B. Schoun, C. Benko, N. Dörre, K. L. Corwin, and J. Ye, Phase-matched extreme-ultraviolet frequency-comb generation, *Nature Photon.* **12**, 387 (2018).
- [36] D. R. Miller, in *Atomic and Molecular Beam Methods*, edited by G. Scoles, Vol. 1 (Oxford University Press, Oxford, 1988), Chap. 2, p. 17.
- [37] Ch. Heyl, S. B. Schoun, G. Porat, H. Green, and J. Ye, A nozzle for high-density supersonic gas jets at elevated temperatures, *Rev. Sci. Instrum.* **89**, 113114 (2018).
- [38] J. Nauta, J.-H. Oelmann, A. Borodin, A. Ackermann, P. Knauer, I. S. Muhammad, R. Pappenberger, T. Pfeifer, and J. R. Crespo López-Urrutia, XUV frequency comb production with an astigmatism-compensated enhancement cavity, *Opt. Express* **29**, 2624 (2021).
- [39] J. Schulte, T. Sartorius, J. Weitenberg, A. Vernaleken, and P. Russbueldt, Nonlinear pulse compression in a multi-pass cell, *Opt. Lett.* **41**, 4511 (2016).
- [40] S. Hädrich, J. Rothhardt, M. Krebs, S. Demmler, A. Klenke, A. Tünnermann, and J. Limpert, Single-pass high harmonic generation at high repetition rate and photon flux, *J. Phys. B: At. Mol. Opt. Phys.* **49**, 172002 (2016).
- [41] J. Weitenberg, A. Vernaleken, J. Schulte, A. Ozawa, T. Sartorius, V. Pervak, H.-D. Hoffmann, T. Udem, P. Russbüldt, and T. W. Hänsch, Multi-pass-cell-based nonlinear pulse compression to 115 fs at 7.5  $\mu$ J pulse energy and 300 W average power, *Opt. Express* **25**, 20502 (2017).
- [42] J. Weitenberg, T. Saule, J. Schulte, and P. Rußbüldt, Nonlinear pulse compression to sub-40 fs at 4.5  $\mu$ J pulse energy by multi-pass-cell spectral broadening, *IEEE J. Quant. Elec.* **53**, 8600204 (2017).
- [43] N. Lilienfein, C. Hofer, S. Holzberger, C. Matzer, P. Zimmermann, M. Trubetskov, V. Pervak, and I. Pupeza, Enhancement cavities for few-cycle pulses, *Opt. Lett.* **42**, 271 (2017).
- [44] S. Richter, F. Zimmermann, A. Tünnermann, and S. Nolte, Laser welding of glasses at high repetition rates—Fundamentals and prospects, *Opt. Laser Technol.* **83**, 59 (2016).
- [45] J. Tiedau, M. V. Okhapkin, K. Zhang, J. Thielking, G. Zitzer, E. Peik, F. Schaden, T. Pronebner, I. Morawetz, L. Toscani De Col *et al.*, Laser excitation of the Th-229 nucleus, *Phys. Rev. Lett.* **132**, 182501 (2024).
- [46] R. Elwell, C. Schneider, J. Jeet, J. E. S. Terhune, H. W. T. Morgan, A. N. Alexandrova, H. B. Tran Tan, A. Derevianko, and E. R. Hudson, Laser excitation of the  $^{229}\text{Th}$  nuclear transition in a solid-state host, *Phys. Rev. Lett.* **133**, 013201 (2024).
- [47] C. Zhang, T. Ooi, J. S. Higgins, J. F. Doyle, L. von der Wense, K. Beeks, A. Leitner, G. A. Kazakov, P. Li, P. G. Thirolf, T. Schumm, and J. Ye, Frequency ratio of the  $^{229\text{m}}\text{Th}$  nuclear isomeric transition and the  $^{87}\text{Sr}$  atomic clock, *Nature (London)* **633**, 63 (2024).
- [48] P. Russbueldt, D. Hoffmann, M. Höfer, J. Löhring, J. Luttmann, A. Meissner, J. Weitenberg, M. Traub, T. Sartorius, D. Esser *et al.*, Innoslab amplifiers, *IEEE J. Sel. Top. Quantum Electron.* **21**, 447 (2015).
- [49] D. Esser, J. Weitenberg, W. Bröring, I. Pupeza, S. Holzberger, and H.-D. Hoffmann, Laser-manufactured mirrors for geometrical output coupling of intracavity-generated high harmonics, *Opt. Express* **21**, 26797 (2013).